A&A 669, A136 (2023)
https://doi.org/10.1051/0004-6361/202245119

Astronomy & Astrophysics

Gaia-`IGRINS` synergy: Orbits of newly identified Milky Way star clusters

Elisa R. Garro[1], José G. Fernández-Trincado[2], Dante Minniti[1,3], Wisthon H. Moya[2], Tali Palma[4], Timothy C. Beers[5], Vinicius M. Placco[6], Beatriz Barbuy[7], Chris Sneden[8], Alan Alves-Brito[9], Bruno Dias[10], Melike Afşar[11], Heinz Frelijj[2], and Richard R. Lane[12]

[1] Instituto de Astrofísica, Facultad de Ciencias Exactas, Universidad Andrés Bello, Fernández Concha 700, Las Condes, Santiago, Chile
e-mail: `elisaritagarro1@gmail.com`
[2] Instituto de Astronomía, Universidad Católica del Norte, Av. Angamos 0610, Antofagasta, Chile
[3] Vatican Observatory, 00120 Vatican City State, Italy
[4] Observatorio Astronómico, Universidad Nacional de Córdoba, Laprida 854, 5000 Córdoba, Argentina
[5] Department of Physics and Astronomy and JINA Center for the Origin of the Elements (JINA-CEE), University of Notre Dame, Notre Dame, IN 46556, USA
[6] NSF's NOIRLab, 950 N. Cherry Ave., Tucson, AZ 85719, USA
[7] Universidade de São Paulo, IAG, Rua do Matão 1226, Cidade Universitária, São Paulo 05508-900, Brazil
[8] Department of Astronomy and McDonald Observatory, The University of Texas, Austin, TX 78712, USA
[9] Universidade Federal do Rio Grande do Sul, Instituto de Física, Av. Bento Gonçalves 9500, Porto Alegre, RS, Brazil
[10] Instituto de Alta Investigación, Sede Esmeralda, Universidad de Tarapacá, Av. Luis Emilio Recabarren 2477, Iquique, Chile
[11] Department of Astronomy and Space Sciences, Ege University, 35100 Bornova, İzmir, Turkey
[12] Centro de Investigación en Astronomía, Universidad Bernardo O'Higgins, Avenida Viel 1497, Santiago, Chile

Received 2 October 2022 / Accepted 29 November 2022

ABSTRACT

Context. The recent and exquisite astrometric, photometric, and radial velocity measurements of the *Gaia* mission resulted in a substantial advancement of the determination of the orbits for old star clusters, including the oldest Milky Way globular clusters (MW GCs).

Aims. The main goal of the present paper is to use the new *Gaia* data release 3 (DR3) and the VISTA Variables in the Via Láctea Extended Survey (VVVX) measurements to obtain the orbits for nearly a dozen new MW GC candidates that have been poorly studied or previously unexplored.

Methods. We use the *Gaia* DR3 and VVVX databases to identify bona fide MW GC candidates, namely VVV-CL160, Patchick 122, Patchick 125, Patchick 126, Kronberger 99, Kronberger 119, Kronberger 143, ESO 92-18, ESO 93-08, *Gaia* 2, and Ferrero 54. The relevant mean cluster physical parameters are derived (distances, Galactic coordinates, proper motions, radial velocities). We also measure accurate mean radial velocities for the GCs VVV-CL160 and Patchick 126 using observations acquired at the Gemini-South telescope with the Immersion GRating INfrared Spectrometer (IGRINS) high-resolution spectrograph. Orbits for each cluster are then computed using the `GravPot16` model, assuming typical Galactic bar pattern speeds.

Results. We reconstruct the orbits for these 11 star clusters for the first time. These include star clusters with retrograde and prograde orbital motions, both in the Galactic bulge and disk. We obtain orbital properties for this sample, such as the mean time-variations of perigalactic and apogalactic distances, eccentricities, vertical excursions from the Galactic plane, and Z-components of the angular momentum.

Conclusions. Our main conclusion is that, based on the orbital parameters, Patchick 125 and Patchick 126 are genuine MW bulge or halo GCs; and Ferrero 54, *Gaia* 2, and Patchick 122 are MW disk GCs. In contrast, the orbits of Kronberger 99, Kronberger 119, Kronberger 143, ESO 92-18, and ESO 93-08 are more consistent with old MW disk open clusters, in agreement with previous results. VVV-CL160 falls very close to the Galactic centre, but reaches larger distances beyond the Solar orbit, and therefore its origin is still unclear.

Key words. Galaxy: kinematics and dynamics – Galaxy: bulge – Galaxy: disk – globular clusters: general

1. Introduction

Globular clusters (GCs) are powerful time capsules allowing us to reconstruct the history of our Milky Way (MW) galaxy, as well as those of nearby external galaxies. As GCs are some of the oldest objects in our MW, we expect them to help us characterise the assembly history of our Galaxy, especially during its early stages, providing clues about its growth through subsequent merger events (Pfeffer et al. 2017; Forbes et al. 2018). In this context, the Λ cold dark matter cosmological paradigm (e.g., Cole et al. 2000; Robertson et al. 2005; Springel et al. 2006) suggests that the formation of larger galaxies that we observe today proceeds in a bottom-up fashion, meaning that small structures merge together to build up more massive objects. Indeed, we consider GCs to be good laboratories for understanding the formation mechanisms of the MW, because some of them are formed in situ, while others are formed in different progenitors (such as dwarf galaxies) before being accreted by the MW, as is already widely accepted. Aside from parameters such as age and metallicity, kinematic information can also help us to model the origin of GCs (Minniti 1995). Broadly, young and metal-poor GCs show halo-like kinematics, while young and metal-rich GCs exhibit disk-like kinematics. Additionally, it is probable that the halo-like clusters have been accreted, meaning that their origin is ex situ, whereas the disk-like ones formed in situ (e.g., Recio-Blanco 2018). Recently, Chen & Gnedin (2022) investigated the origin of GCs using simulations, which suggested that in situ GCs form in the main progenitor branch of a given galaxy, while ex situ GCs form in satellite galaxies and are later accreted. These latter authors also proposed that GCs of in situ origin are systematically more concentrated towards the Galactic centre, while ex situ GCs are found at larger radii, out to 100 kpc. Moreover, the in situ GCs are significantly more metal-rich than their ex situ counterparts due to the mass–metallicity relation of their host galaxies.

However, the number of known Galactic GCs appears to be low compared to other comparable spiral galaxies (e.g., the Andromeda galaxy), especially in the Galactic bulge (at Galactocentric distances $R_G \lesssim 3.5$ kpc), where approximately 40 GCs are found (see e.g., Barbuy et al. 2018). This is mainly due to: (i) interstellar dust, which stands between us and the inner regions of the Galaxy (Gonzalez et al. 2012; Barbuy et al. 2018); (ii) the small sizes and low luminosities of many hidden GCs (Minniti et al. 2017, 2021; Garro et al. 2021, 2022a,b), probably because they have survived strong dynamic processes typical of those regions (Kruijssen et al. 2011); and (iii) very high field crowding, making their detection challenging.

Regardless, many new GCs have recently been uncovered in the MW bulge and disk (see e.g., Minniti et al. 2017, 2019; Ramos et al. 2018; Gran et al. 2019, 2022; Garro et al. 2021, 2022a,b) thanks to deep near-infrared (NIR) surveys, such as the VISTA variables in the Via Láctea and its extensions (VVV/VVVX; Minniti et al. 2010; Saito et al. 2012) surveys, allowing for penetration of dense columns of gas and dust and extremely dense regions. These surveys are, in turn, highly complemented by precise astrometry provided by the novel ESA *Gaia* space mission (Gaia Collaboration 2021, 2023).

Taking advantage of these exquisite datasets, a recent collection of publications by Garro et al. (2020, 2021, 2022a,b) has provided in-depth photometric characterisation of 34 selected Galactic GC candidates towards the bulge and inner disk regions. However, detailed kinematical information is still lacking for these potential older systems in the MW. The present study is the first attempt to determine the kinematics of a handful of these newly revealed GC systems and to provide a dynamical characterisation.

Here, we present a kinematic and orbital study of 11 selected star clusters (Table 1). The paper is organised as follows: Sect. 2 introduces our observations and data for the two GCs, VVV-CL160 and Patchick 126, acquired with the Immersion GRating INfrared Spectrometer (IGRINS), and for another nine GCs in the *Gaia* images. In Sect. 2.1, radial velocities (RVs) are derived for the stars of each selected cluster using the observed NIR spectra. The *Gaia* DR3 dataset used to derive the main physical parameters for those GCs with suitable RVs is described in Sect. 2.4. We reconstructed the cluster orbits, as explained in Sect. 3, in order to characterise the origin of each cluster, as detailed in Sect. 4. Finally, a summary and concluding remarks are presented in Sect. 5.

2. Observations and data

We selected the brightest stars in the close vicinity of VVV-CL160 and Patchick 126, two bulge GC candidates newly discovered by Garro et al. (2022b) and Garro et al. (2022a), respectively. Our aim is to provide mean RVs and dynamical properties for these two systems and nine other selected GCs in the *Gaia* footprint. We obtained NIR RV determinations for VVV-CL160 and Patchick 126, as described in Sect. 2.1, and investigated mean *Gaia* RVs for nine other GCs, as outlined in Sect. 2.4. The only cluster for which we have both IGRINS and *Gaia* information is Patchick 126.

2.1. IGRINS/Gemini-South observations

We carried out IR spectroscopic follow-up investigations for a total of 16 potential brightest ($K_s < 12$) red giant branch (RGB) members towards two newly identified GC candidates: VVV-CL160 and Patchick 126. Cluster memberships were originally selected on the basis of distance from the GC centre, *Gaia* proper motions, and position on the colour–magnitude diagram (CMD).

The observations were executed in queue mode over seven nights between February 2022 and April 2022 under the program `GS-2022A-Q-132`, and over three nights in April 2022 under the program `GS-2022A-Q-238` (PI: Elisa R. Garro), using the visiting high-resolution ($R \sim 45\,000$) IGRINS installed on the 8.1m Gemini-South telescope at Cerro Pachón, Chile. IGRINS[1] is a cross-dispersed spectrograph with two separate arms covering the H- and K-bands, providing a spectral coverage of 1.45–2.45 μm at a spectral resolution of $R \sim 45\,000$ (Park et al. 2014; Mace et al. 2018). Each observed spectrum was taken in an ABBA nod sequence along the slit, together with a nearby A0V telluric standard star. We summarise the observational aspects for each target in Table 2. In the following, we further detail the main characteristics of the GC targets observed with the IGRINS spectrograph.

2.1.1. VVV-CL160

Studied by Minniti et al. (2021) and Garro et al. (2022b), VVV-CL160 was identified in the VVV footprint towards α = 18:06:57.0 and $\delta = -20$:00:40 at a heliocentric distance $D_\odot = 6.8 \pm 0.5$ kpc and at $R_G = 1.92 \pm 0.4$ kpc from the Galactic centre. As analysed by Garro et al. (2022b), this cluster was also found to be heavily affected by high extinction ($A_V \sim 5.68$ mag, Lallement et al. 2022), while the isochrone fits of its CMDs suggested that it is likely a metal-poor ([Fe/H] = −1.4) and old (age ∼ 12–13 Gyr) GC, with an apparent low luminosity ($M_V \approx -5.5$ mag), but interestingly, with extreme proper motions ($\mu_{\alpha_*}; \mu_\delta = -2.90; -16.47$ mas yr^{-1}; Table 1). We collected IGRINS spectra for 12 potential member RGB stars located within 3′ of the centre of VVV-CL160, with a typical $S/N > 50$ pixel^{-1}, which allowed us to provide an accurate observed RV (RV $\approx 245.3 \pm 0.8$ km s^{-1}) estimate for VVV-CL160 for the first time (see Sect. 2.3).

2.1.2. Patchick 126

Examined for the first time by Garro et al. (2022a), Patchick 126 was identified in the VVV footprint towards $\alpha = 17:05:38.6$ and $\delta = -47:20:32$, at heliocentric distance $D_\odot = 8.0 \pm 0.5$ kpc

---

[1] `https://sites.google.com/site/igrinsatgemini/overview`

Table 1. Main physical parameters for our cluster sample using a combination of the *Gaia* DR3, 2MASS, and VVV/VVVX datasets, which are in agreement with those determined by Garro et al. (2022a,b).

Cluster	RA [hh:mm:ss]	Dec [dd:mm:ss]	μ_{α_*} [mas yr^{-1}]	μ_δ [mas yr^{-1}]	$D_\odot$ [kpc]	R_G [kpc]	Age [Gyr]	[Fe/H]
VVV-CL160	18:06:57.0	−20:00:40	-2.90 ± 1.28	-16.47 ± 1.31	6.8 ± 0.5	1.93	13.0 ± 2.0	-1.4 ± 0.3
Patchick 126	17:05:38.6	−47:20:32	-4.96 ± 0.40	-6.80 ± 0.40	8.0 ± 0.5	2.82	>8.0	-0.7 ± 0.3
Patchick 122	09:42:30.7	−52:25:41	-3.92 ± 0.40	3.62 ± 0.40	5.1 ± 1.0	9.17	10.0 ± 3.0	-0.5 ± 0.2
Patchick 125	17:05:00.7	−35:29:41	-3.84 ± 0.39	0.65 ± 0.39	11.1 ± 1.0	3.41	14.0 ± 2.0	-1.8 ± 0.2
Kronberger 99	09:11:17.6	−46:23:27	-3.67 ± 0.30	4.42 ± 0.31	4.1 ± 1.0	9.26	8.0 ± 2.0	-0.8 ± 0.2
Kronberger 119	10:47:15.7	−63:19:42	-3.96 ± 0.39	1.79 ± 0.40	10.6 ± 1.0	11.03	6.0 ± 1.0	-0.6 ± 0.1
Kronberger 143	11:57:42.6	−64:10:40	-7.65 ± 0.40	0.66 ± 0.40	6.4 ± 1.0	7.77	6.0 ± 1.0	-0.6 ± 0.2
ESO 92-18	10:14:55.2	−64:36:40	-3.60 ± 0.32	2.69 ± 0.32	10.1 ± 1.0	10.99	5.0 ± 1.0	-0.9 ± 0.2
ESO 93-08	11:19:41.9	−65:13:11	-4.07 ± 0.03	1.40 ± 0.03	13.57 ± 1.0	12.76	>5.0	-0.4 ± 0.2
Gaia 2	01:52:33.0	+53:02:36	-1.32 ± 0.33	1.21 ± 0.33	4.7 ± 1.0	11.85	10.0 ± 1.0	-0.9 ± 0.2
Ferrero 54	08:33:48.3	−44:26:49	-1.39 ± 0.37	1.22 ± 0.37	7.2 ± 1.0	11.57	11.0 ± 1.0	-0.3 ± 0.2

and Galactocentric distance $R_G = 2.82 \pm 0.5$ kpc. Patchick 126 exhibits a well-defined RGB and a poorly populated red clump in the CMD, which were used to fit isochrone models and derive age and metallicity. These latter authors estimated a mean metallicity [Fe/H] $= -0.7 \pm 0.3$ and an approximate age of greater than 8 Gyr. The extinction of this cluster is $A_V \sim 0.44$ mag in the NIR, and its proper motions ($\mu_{\alpha_*}; \mu_\delta = -4.75;\ -6.68$ mas yr^{-1}; Table 1) are commensurate with those of bulge GCs. As explained in Sect. 2.4, we re-analysed Patchick 126 using a combination of the optical *Gaia* DR3 and the NIR VVVX datasets, obtaining similar results to those of Garro et al. (2022a). Furthermore, we collected IGRINS spectra for four RGB stars within 0.9′ of the centre of Patchick 126, with a typical $S/N > 50$ pixels^{-1}, from which we provide the first RV estimate for this object of -121.8 ± 0.3 km s^{-1} (see Sect. 2.3).

2.2. Data reduction and processing

The IGRINS spectra were reduced and processed with the IGRINS reduction pipeline package[2] (PLP; Lee et al. 2017). The PLP performs flat fielding, subtraction of the A and B images (A–B) to efficiently remove sky background, wavelength calibration using OH emission and telluric lines, and extraction of an appropriate 1D spectrum based on the technique of Horne (1986). The 28th and 26th orders for the *H* and *K* arms, respectively, were combined into a single continuous spectrum. After merging the orders, we performed the continuum normalisation and removal of telluric lines using IRAF[3] packages (`continuum, sarith`). The wavelength scales of these spectra were then converted from vacuum into air using the recommended transformation by the `IGRINS PLP`[4].

An example of the final spectra is shown in Fig. 1 for the *H*- and *K*-band wavelengths, respectively. We show spectra of four RGB stars, each of which has been wavelength calibrated, continuum normalised, cleaned of telluric lines, and merged into a single continuous spectrum. It is notable that high resolution and high S/N both in the *H*- and *K*-band spectra of these RGB stars reveal a rich assortment of atomic and molecular features.

2.3. IGRINS/Gemini-South radial velocities

The RV of each star was determined by cross-correlation against a template spectrum obtained from the MOOG[5] synthetic spectrum code (Sneden 1973) in the spectral regions of IGRINS spectra available in the `iSpec`[6] open source framework (Blanco-Cuaresma et al. 2014; Blanco-Cuaresma 2019). We also adopted model atmospheres from the `APOGEE.ATLAS9` database (Mészáros et al. 2012) in order to construct the solar template, and used it to perform the cross-correlation and derive suitable RVs. In the same manner, we synthesised another template with similar characteristics of red giant stars. As we have not yet derived the atmospheric parameters of our stars, we assumed similarities with the well-known Arcturus star, with $T_{\rm eff} = 4286$ K, $\log g = 1.66$ cgs, [Fe/H] $= -0.5$, and spectral type K0III. Figure 2 shows how the positions of the atomic and molecular lines are the same in both the *H*-band and *K*-band for both templates. The main discrepancies concern the depths of the lines, and these are due to the different temperature, gravity, metallicity, and micro- and macro-turbulent velocity. We derived RVs using these two templates, finding the same results. Additionally, we corrected the observed spectrum to the rest frame. Figure 3 displays the observed *H*- and *K*-band spectra for two representative RGB stars in VVV-CL160 and Patchick 126, where we superimpose the solar template in order to show which spectral lines are used for the cross-correlation. We separately estimated RVs from the *H*- and *K*-band spectra and then Doppler-corrected each spectrum. We note that the difference in RV between H- and K- band spectra is smaller than 0.5 km s^{-1}. The heliocentric RVs listed in Table 3 are the average of the two values. The RV errors are calculated following Zucker (2003):

$$\sigma^2_{\rm RV} = -\left[N \frac{C''(v)}{C(v)} \frac{C^2(v)}{1 - C^2(v)}\right]^{-1}, \tag{1}$$

where N is the number of bins in the spectrum, C is the cross-correlation function, and C'' is its second derivative. Also, we estimated signal-to-noise ratios (S/Ns) for *H*- and *K*-band spectra adopting the variances obtained by the PLP during the data-reduction process. The S/Ns for *H*- and *K*-band spectra are listed separately in Table 2; all are $S/N \gtrsim 85$, which is sufficient for deriving robust RV estimates.

---

[2] `https://github.com/igrins/plp`

[3] Image Reduction and Analysis Facility (IRAF), was distributed by the National Optical Astronomy Observatory, which was managed by the Association of Universities for Research in Astronomy (AURA) under a cooperative agreement with the National Science Foundation.

[4] `https://igrinscontact.github.io/RRISA_reduced/`

[5] `https://www.as.utexas.edu/~chris/moog.html`

[6] `https://www.blancocuaresma.com/s/iSpec`

Table 2. Program star parameters and observations with IGRINS spectrograph for VVV-CL160 and Patchick 126 GCs.

Nstar	ID [a]	RA [hh:mm:ss]	Dec [dd:mm:ss]	K [a] [mag]	μ_{α_*} [b] [mas yr^{-1}]	μ_{δ} [b] [mas yr^{-1}]	μ_{α_*} [c] [mas yr^{-1}]	μ_{δ} [c] [mas yr^{-1}]	Date [d] (2022)	Exposure (s)	S/N_H	S/N_K
Program `GS-2022A-Q-132`: VVV-CL160												
Star 1	18064691-1959488	18:06:46.90	−19:59:49.1	11.633	−2.932	−16.116	−1.411	−16.603	February 24	183.25	101.32	98.42
Star 2	18070670-2002077	18:07:06.70	−20:02:08.0	11.099	−3.010	−16.964	−0.596	−15.169	March 13	112.0	100.30	85.86
Star 2 [*]	18070670-2002077	18:07:06.70	−20:02:08.0	11.099	−3.010	−16.964	−0.596	−15.169	March 26	112.0	121.59	114.31
Star 3	18065665-2003009	18:06:56.66	−20:03:01.2	11.345	−2.361	−15.795	−4.593	−14.506	April 22	140.5	110.00	103.67
Star 4	18070130-2001160	18:07:01.30	−20:01:16.4	11.316	−2.815	−17.005	−2.608	−16.629	March 18	136.75	107.47	95.18
Star 5	18065353-2001165	18:06:53.53	−20:01:16.8	10.815	−0.787	−16.942	−1.531	−16.253	March 18	86.25	115.31	98.93
Star 6	18070452-2001590	18:07:04.52	−20:01:59.4	11.389	−2.964	−16.453	–	–	April 22	146.25	113.13	100.18
Star 7	18065450-2001040	18:06:54.50	−20:01:04.4	10.882	−2.565	−17.007	−2.504	−16.415	April 23	91.75	122.14	117.53
Star 8	18065275-2000396	18:06:52.74	−20:00:39.9	11.449	−2.462	−16.900	−2.628	−15.794	March 26	154.5	113.42	120.00
Star 9	18070303-2000482	18:07:03.03	−20:00:48.5	11.618	−2.627	−16.417	−1.326	−17.425	March 26	180.75	129.45	111.31
Star 10	18070135-2002466	18:07:01.35	−20:02:46.8	11.759	−2.799	−16.489	–	–	March 25	205.75	107.98	95.16
Star 11	18065905-2000323	18:06:59.05	−20:00:32.7	10.168	−3.745	−18.010	−1.597	−16.566	March 25	47.5	108.49	97.66
Star 12	18065973-1959460	18:06:59.73	−19:59:46.3	10.066	−1.722	−17.089	−2.229	−17.151	March 26	43.25	110.66	120.04
Program `GS-2022A-Q-238`: Patchick 126												
Star 1	7053569-4720154	17:05:35.68	−47:20:15.5	12.310	−5.298	−6.875	−4.807	−7.026	April 2	341.75	157.85	157.11
Star 2	7053688-4720019	17:05:36.88	−47:20:02.2	10.991	−5.123	−6.359	−4.711	−6.388	April 2	101.5	166.02	141.05
Star 3	7054018-4720297	17:05:40.14	−47:20:29.8	11.917	−4.626	−6.882	−5.018	−6.664	April 23	238.0	156.15	162.83
Star 4	7053909-4720359	17:05:39.10	−47:20:36.1	12.435	−4.384	−6.369	−4.995	−7.101	April 20	383.5	128.64	128.78

Notes. [*]Repeated observation. [a]From the 2MASS (Skrutskie et al. 2006). [b]From the VVVX (Minniti et al. 2010; Saito et al. 2012). [c]From the *Gaia* Data Release 3 (Gaia Collaboration 2016, 2023). [d]Date of IGRINS observations.

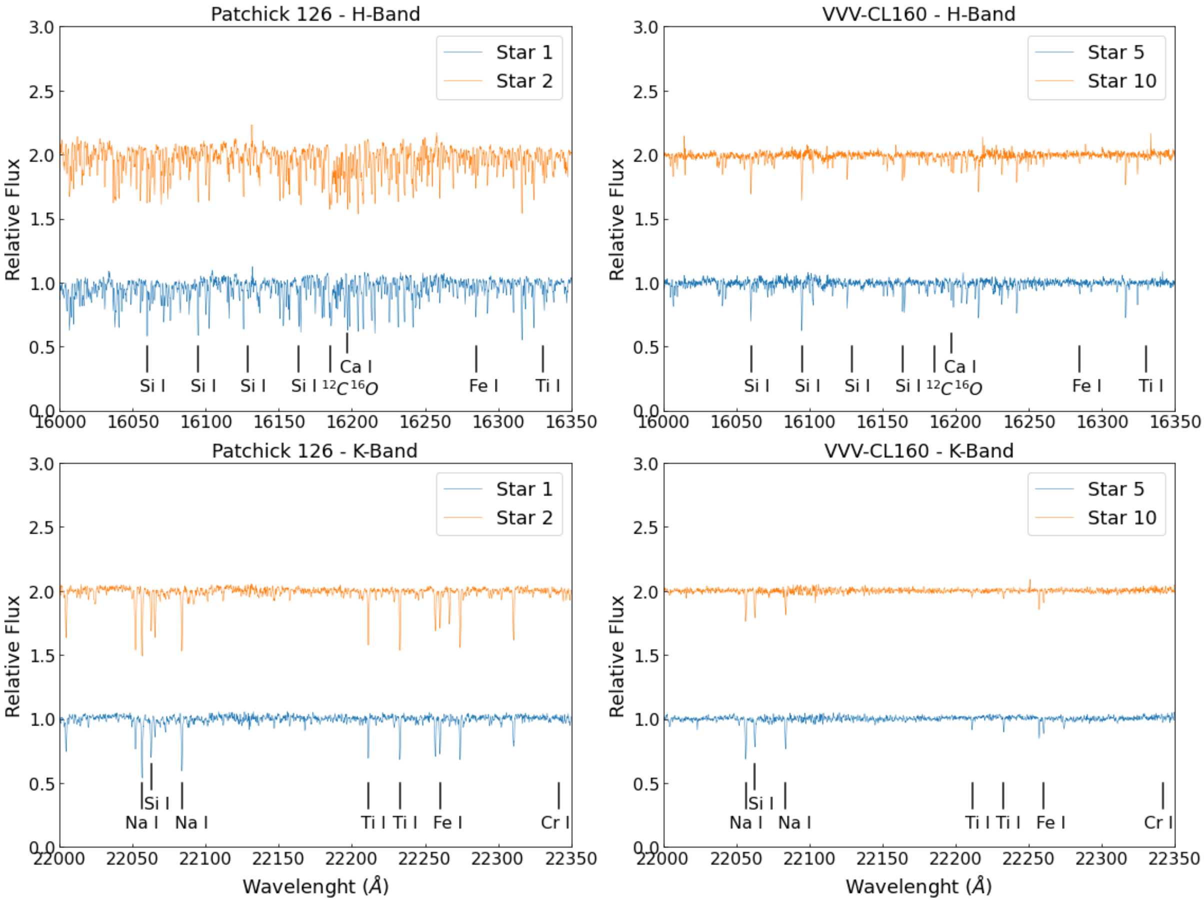

Fig. 1. Final IGRINS spectra. Representative IGRINS *H*- and *K*-band spectra of two RGB stars in each GC in air wavelengths: Star 1 and Star 2 for Patchick 126 (*left panels*), and Star 5 and Star 10 for VVV-CL160 (*right panels*). For clarity in the plot, we have shifted the relative flux scale of Star 2 and Star 10 vertically with additive constants, and show zoomed spectra between 16 000 and 16 350 Å in the *H*-band and between 22 000 and 22 350 Å in the *K*-band. We identified some spectral features (Si I, Ca I, Na I, Fe I, Ti I and $C^{12}O^{16}$).

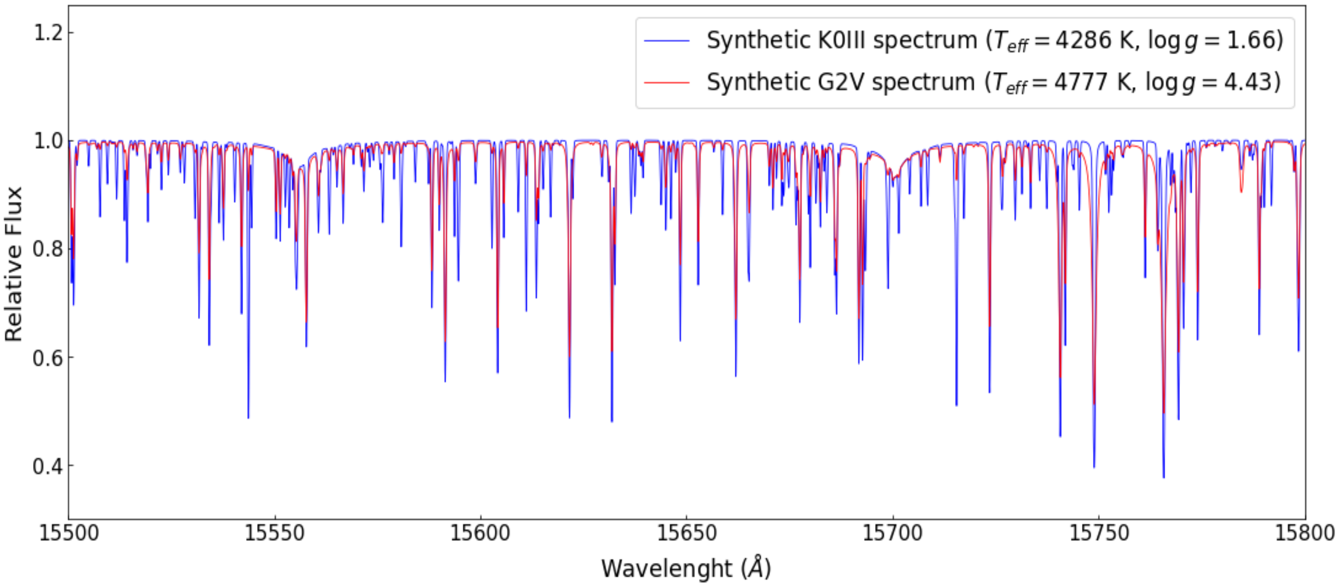

Fig. 2. Synthetic spectra. Comparison between spectra for Arcturus and the Sun.

All 12 stars identified as the highest likelihood members for VVV-CL160 have measured RVs of between 241.85 km s^{-1} and 251.22 km s^{-1}, suggesting an average systematic RV for VVV-CL160 of 245.57 ± 0.58 km s^{-1} in the *H*-band, and 245.03 ± 0.56 km s^{-1} in the *K*-band. For Patchick 126, we derived minimum and maximum RVs of −118.54 km s^{-1} and −122.99 km s^{-1}, respectively, without RV dispersion. We determine a systematic value of RV for the cluster of −121.81 ± 0.25 km s^{-1} in the *H*-band and −121.83 ± 0.25 km s^{-1} in the *K*-band. Based on positions, PMs, RVs, and the high and low RV scatters of our sample, we can confirm that all the selected targets are bona fide cluster members of VVV-CL160 and Patchick 126.

Finally, we give a crude estimation of the mass for these two clusters, even if a larger number of member RVs are needed. We first derived the velocity dispersion (σ) both in the *H*- and *K*-band, but the mean of the two values is adopted. We then assumed that the angular radii of 3′ for VVV-CL160 and 0.9′ for Patchick 126 found by Garro et al. (2022a,b) are the physical sizes of the clusters. Therefore, we obtained a physical radius of $R \sim 5.9$ pc for VVV-CL160 and $R \sim 2.0$ pc for Patchick 126 at their distances. Thereafter, we used the following equation to derive masses:

$$M = \frac{3}{2}\frac{\sigma^2 R}{G}, \tag{2}$$

where G is the gravitational constant of 6.6743×10^{-11} m^3 kg^{-1} s^{-2}. We derived an approximate mass of $M \approx 6.8 \times 10^4\, M_\odot$ for VVV-CL160 and $M \approx 2.4 \times 10^3\, M_\odot$ for Patchick 126. IGRINS elemental abundances for both VVV-CL160 and Patchick 126 stars will be extensively presented in a separate contribution.

2.4. Gaia DR3 data

In recent contributions by Garro et al. (2022a,b), many new cluster candidates were photometrically analysed. These authors suggested that the candidate objects are real GCs or old open clusters (OCs) located in the Galactic bulge and disk. As these are newly uncovered and low-luminosity objects, kinematic information was not available from either spectroscopy or existing surveys, and so the authors were unable to confirm their true nature.

The recent *Gaia* data release 3 (DR3, Gaia Collaboration 2016, 2023) is based on spectra collected over 34 months of the mission. It includes RVs for nearly 34 million stars reaching as faint as G = 14 mag (Katz et al. 2023). The median formal precision of the RVs is ~1.3 km s^{-1} at $G_{\rm RV}$ = 12 and ~6.4 km s^{-1} at $G_{\rm RV}$ = 14. We searched for stars with RVs in the clusters listed in Garro et al. (2022a,b), and found that some of them have good *Gaia* DR3 RVs estimates.

We re-analysed these clusters using the *Gaia* DR3 dataset, and cross-matched the latter with the NIR 2MASS and VVV/VVVX (where possible) datasets. We followed the same decontamination and membership procedures as explained in the previous works by Garro et al. (2022a,b). In summary, we first cleaned all cluster samples of nearby stars through a cut in parallax. Deriving the size of our clusters was a difficult task because of the low luminosity of our targets and high stellar density of these regions. However, we carried out two distinct methods in order to fix the dimension of the clusters: (i) inspection of the density diagrams as a function of sky position and (ii) application of the Gaussian kernel density estimate (KDE; e.g., Parzen 1962) in order to fit isodensity contours (see Figures 2 and 3 in Garro et al. 2022a). By balancing these two methods, we selected stars within a given radius. We adopted a GC radius of $r \sim 3'$ for VVV-CL160, Kronberger 99, Kronberger 143, Ferrero 54, ESO 92-18, and *Gaia* 2, and a larger size of $r \sim 4.2'$ for ESO 93-08, and smaller dimensions $r < 2.5'$ for Kronberger 119, Patchick 122, Patchick 125, and Patchick 126. A third selection criterion concerned the PMs: we only included stars with PMs $\lesssim$1 mas yr^{-1} from the mean cluster PM and with PM probability >50% (see Fig. B.1. in Garro et al. 2022a). We were able to estimate the mean cluster PMs using the σ-clipping technique. Once decontaminated optical (G versus BP-RP) and NIR (K_s versus $J - K_s$) CMDs were constructed (Fig. A.1), we derived the main physical parameters, such as reddening, extinction, and distance modulus. Ages and metallicity were obtained by performing isochrone fitting. We adopted the PARSEC models (Bressan et al. 2012; Marigo et al. 2017), as in our previous works. We obtained very similar results to the Garro et al. values, which are listed in Table 1. Depending on

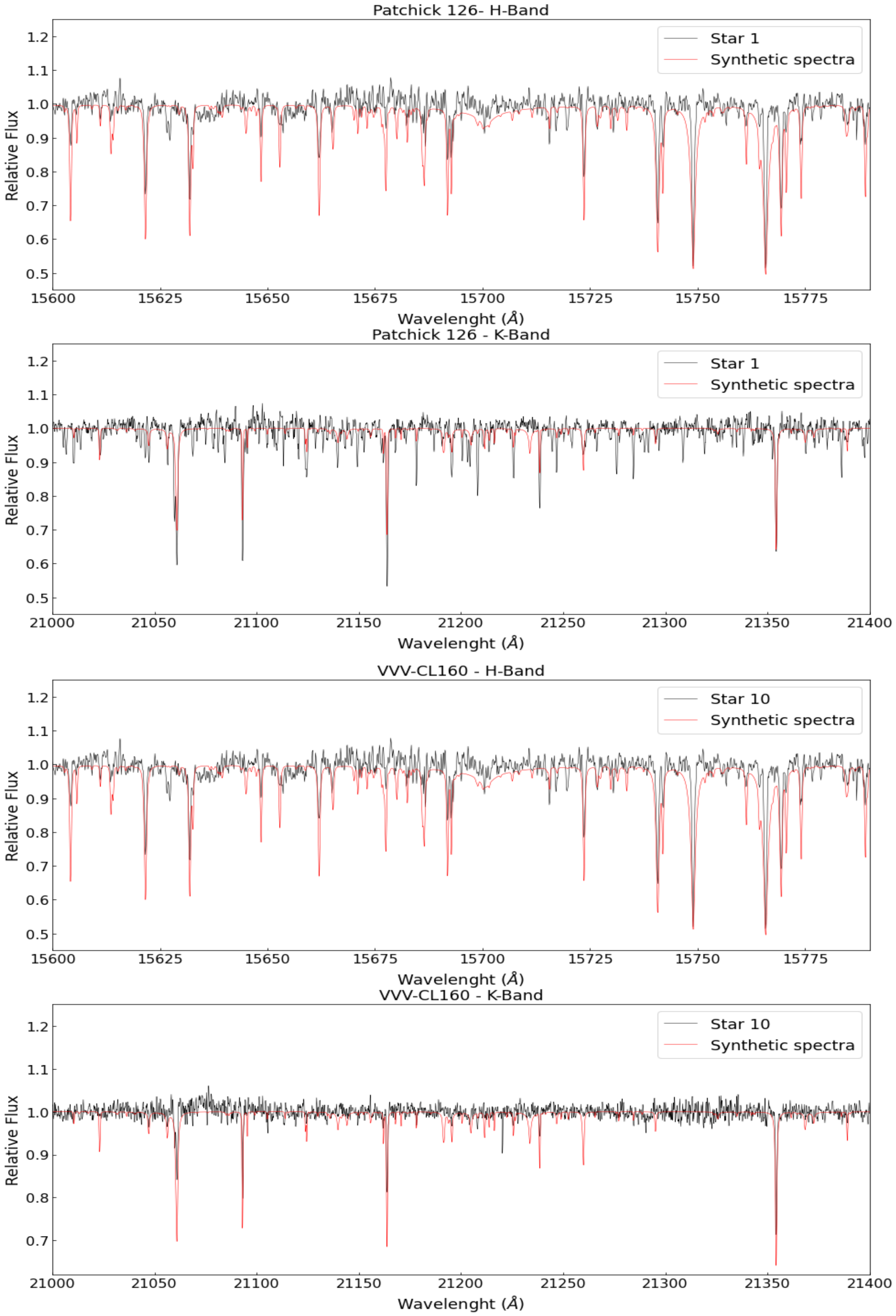

Fig. 3. Cross-correlation. Representative IGRINS *H*- and *K*-band spectra of two RGB stars: Star 1 for Patchick 126 and Star 10 for VVV-CL160 (black lines). We superimposed the synthetic solar spectra (red lines) used for determination of cross-correlation velocities in the spectral regions between 15 000 and 17 000 Å in the *H*-band, and between 19 500 and 22 900 Å in the *K*-band.

Table 3. Kinematical properties of the GCs VVV-CL160 and Patchick 126 observed with the IGRINS spectrograph.

Nstar	$V_{\rm helio}$ [km s^{-1}]	RV$_H$ [km s^{-1}]	$\sigma_{{\rm RV}_H}$ [km s^{-1}]	RV$_K$ [km s^{-1}]	$\sigma_{{\rm RV}_K}$ [km s^{-1}]
Program `GS-2022A-Q-132`: VVV-CL160					
Star 1	27.28	246.82	0.69	246.00	0.59
Star 2	29.69	248.48	0.63	248.08	0.65
Star 2 (*)	29.84	249.04	0.66	248.53	0.63
Star 3	25.48	241.85	0.61	241.60	0.61
Star 4	29.98	245.54	0.61	245.15	0.62
Star 5	29.94	245.43	0.46	244.88	0.46
Star 6	25.40	243.64	0.51	243.88	0.51
Star 7	25.40	242.05	0.54	241.50	0.52
Star 8	29.96	247.41	0.75	246.58	0.71
Star 9	29.92	244.43	0.56	243.59	0.56
Star 10	29.90	251.22	0.55	250.44	0.53
Star 11	29.91	241.53	0.48	240.64	0.44
Star 12	29.87	245.01	0.45	244.53	0.42
mean		245.57		245.03	
error		0.58		0.56	
VVV-CL160 RV = 245.30 ± 0.81 km s^{-1}					
Program `GS-2022A-Q-238`: Patchick 126					
Star 1	20.91	−122.86	0.24	−122.67	0.25
Star 2	20.83	−122.95	0.25	−122.85	0.25
Star 3	19.60	−122.99	0.22	−122.96	0.25
Star 4	20.74	−118.45	0.27	−118.85	0.25
mean		−121.81		−121.83	
error		0.25		0.25	
Patchick 126 RV = -121.82 ± 0.35 km s^{-1}					

Notes. (*)Repeated observation.

age and metallicity, we provide indications of their nature (GC or OC). However, understanding the nature of clusters such as Kronberger 119 and Kronberger 143 is not straightforward. Indeed, we suggest that they are young GCs or old OCs. The typical age of a GC is greater than 10 Gyr, but there are younger GCs (e.g., Segue 3, Palomar 4; Ortolani et al. 2013, Frank et al. 2012) than the 'classical' ones, with the same metallicity (e.g., Dotter et al. 2010). On the other hand, the typical age of OCs is less than 6–7 Gyr. Nevertheless, there are old OCs with older ages, such as Be 17 and NGC 6791 (age > 9 Gyr, Salaris et al. 2004). A complete CMD, including stars from the main sequence to the evolved sequences, is likely needed to derive precise age, mass, and radius estimations for our clusters in order to better constrain their nature.

Subsequently, we searched for stars with *Gaia* RVs. We matched the decontaminated cluster catalogues with the catalogues containing RVs, and selected stars within 3′ and with a PM matching the mean cluster PM. However, we note that not all stars with similar position and PM showed consistent RV values, and therefore in order to take a conservative approach, we excluded a few RVs that were very different from the average and those with large errors ($>3\sigma$), as shown in Fig. 4. Therefore, depending on our selection, we estimated the number ratio of the RV outliers ($N_{\rm out}$) to the RVs included in our work ($N_{\rm in}$), finding $N_{\rm out}/N_{\rm in} \approx 0.6 - 0.8$. This suggests that more than 60% of our sample is made up of real cluster members, excluding those with lower probability. However, we cannot completely exclude the possibility that some of these outliers could be members, since they may be binaries and therefore display different RVs. We evaluate that the percentage of RV outliers is negligible (1%–2%). We then derived the mean cluster RV as an average of the RVs of each member star. The entire sample of stars with *Gaia* DR3 RVs is listed in Table 4, where we indicate the source identification, coordinates, proper motions, G-magnitude, RVs, and corresponding errors for each star. Additionally, we specify the mean cluster RV and its errors in bold face. Therefore, for constructing the orbits of our targets, we used RVs of some red giant members to represent the RV of the whole cluster. However, we have to point out that we cannot quantify the fraction of RV variables in our samples. RV variables can be identified either by their high standard deviation in the measurements compared with other stars of comparable magnitude or by changes over a longer baseline for stars for which previous observations are available. Therefore, we cannot definitely rule out binaries because of the low statistics of our data.

3. Orbital elements

In this section, we derive orbital elements for all 12 selected GCs, combining estimated RVs, PMs, and heliocentric distances, and making use of the barred Milky Way potential model provided by the `GravPot16` code[7].

3.1. The Galactic model

As described in Fernández-Trincado et al. (2022), the `GravPot16` code provides the 3D gravitational potential and 3D field forces for a physical 'boxy/peanut' bar structure in the bulge region. It also considers other composite stellar components belonging to the superposition of nine disk components (seven thin and two thick disks) with different scale heights or lengths and different local solar densities. The density profiles provided by the Besançon model (e.g., Robin et al. 2003; Picaud & Robin 2004) are accompanied by the interstellar medium (ISM) component, an oblate Hernquist stellar halo structure, and a dark matter component characterised by an isothermal sphere truncated at $R_{\rm Gal} \sim 150$ kpc.

The structural parameters of our bar model are assumed to have $M = 1.1 \times 10^{10}\,M_\odot$ (Fernández-Trincado et al. 2020), a present day orientation of 20° (Fernández-Trincado et al. 2020), and pattern speed $\Omega_{\rm bar} = 41 \pm 10$ km s^{-1} kpc (Sanders et al. 2019). The employed bar model has scale lengths of $x_0 = 1.46$ kpc, $y_0 = 0.49$ kpc, and $z_0 = 0.39$ kpc, with the semi-major axis of the bar cut-off radius of 3.43 kpc on the x-axis, as provided by the best bar density profile examined in Robin et al. (2012).

For reference, the Galactic convention adopted in this work is as follows: x-axis oriented towards $l = 0°$ and $b = 0°$, y-axis oriented towards $l = 90°$ and $b = 0°$, and a disk that rotates towards $l = 90°$; the velocities are oriented in these directions. Following this convention, the Sun's orbital velocity vectors are $[U_\odot, V_\odot, W_\odot] = [11.1, 12.24, 7.25]$ km s^{-1} (Brunthaler et al. 2011). Finally, the model has been rescaled to the Sun's Galactocentric distance of 8.3 kpc, and the local rotation velocity of 244.5 km s^{-1} (Sofue 2015) is adopted.

3.2. Orbits

For each cluster listed in Table 1, we computed Galactic orbits employing a simple Monte Carlo approach under the Runge-Kutta algorithm of seventh to eighth order developed by Fehlberg (1969). The uncertainties in the input data, such

---

[7] `https://gravpot.utinam.cnrs.fr/`

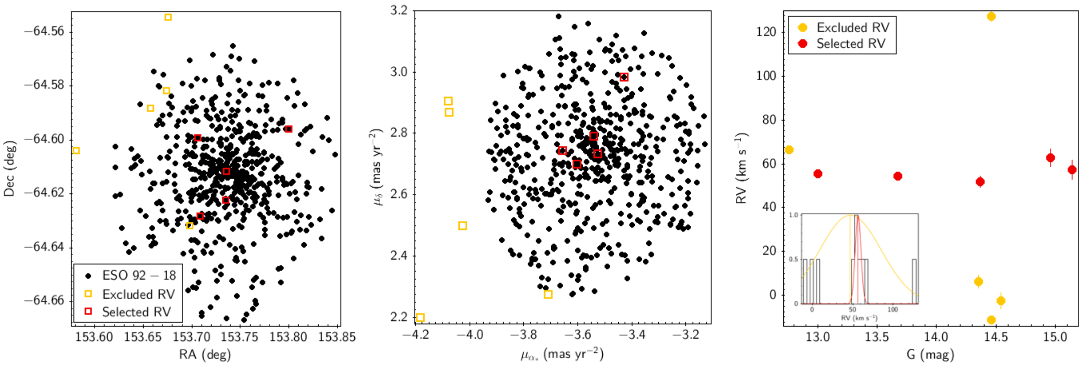

Fig. 4. Selection RVs. We take the cluster named ESO 92-18 as representative, as it is in the direction of this cluster that we identified the highest number of stars with RVs. We show the position (*left panel*) and PM (*in the middle*) diagrams for the PM-selected ESO 92-18 stars (black points) and for stars with RVs. We also display the RV versus *G*-magnitude diagram (*right panel*), where we show selected RV values for those stars that are likely members of the cluster (red points) and those excluded because they show a very different RV with respect to the RV cluster mean. In the insert, we plot the normalised histogram for the sample, and we over-plot the Gaussian fit for the whole sample (yellow line) and for the selected stars (red line), showing how both means and standard deviations change in the two cases.

as coordinates (α, δ), PMs, RVs, and distance errors, were randomly propagated as 1σ variations in a Gaussian Monte Carlo re-sampling. The input RVs that we adopted to reconstruct the orbits are the mean RVs from the RGB members listed in Tables 3 and 4.

The resulting orbital parameters, summarised in Table 5, were determined from ten thousand simulated orbits for each cluster, computed backwards in time for 1.5 Gyr. The 50th percentile of the orbital elements was found for these ten thousand realisations, with the uncertainty ranges given by the 16th and 84th percentiles. We also obtained simulated orbits for three different values of Ω_{bar}, which were varied in steps of 10 km s^{-1} kpc in order to check for any significant impact of variations of this parameter. The minimum and maximum values of the *Z*-component of the angular momentum in the inertial frame are also listed in the same table.

Table 5 and Fig. B.1 show the resulting simulated orbits, and demonstrate that the orbits are not strongly affected by large variations in the assumed bar pattern speed, Ω_{bar}. Figure B.1 displays the probability densities of the resulting ensemble of orbits projected on the equatorial and meridional Galactic planes in the inertial reference frame. The red and yellow colours correspond to more probable regions of space, which are crossed more frequently by our simulated orbits. Moreover, we calculated the minimum and maximum value of the *Z*-component of the angular momentum (L_z) in the inertial frame along the whole integration time for all clusters. As this quantity is not conserved in a model with non-axisymmetric structures such as the MW gravitational potential, we are interested only in the sign in order to verify whether the orbital motion of the GCs is prograde or retrograde with respect to the Galactic rotation. We followed the same analysis and interpretation as in previous works; see for example Fernández-Trincado et al. (2020), Pérez-Villegas et al. (2020), Moreno et al. (2021). As shown in Fig. 5, all GCs exhibit prograde orbits, except for Patchick 125, which is in a retrograde orbit. We present our results in detail for each star cluster in the following subsections.

3.3. ESO 92-18

ESO 92-18 was analysed by Garro et al. (2022a) using a combination of *Gaia* EDR3 and 2MASS datasets. As mentioned above, we analysed it again adopting the recent *Gaia* DR3 dataset, finding similar results to those of these latter authors. ESO 92-18 is a well-populated and young cluster, with an age of 5 ± 1 Gyr and a metallicity of [Fe/H] = −0.9 ± 0.2. We confirm the heliocentric and Galactocentric distances obtained by Garro et al. (2022a): we obtain $D_\odot$ = 10.1 kpc and R_G = 11.0 kpc. From the *Gaia* DR3 catalogue, we identified five member stars with suitable RVs, which are located within ≈4′ of the cluster centre and with PMs within 1 mas yr^{1}. There are a couple of stars with higher errors than the others (as well as in the Kronberger 119 case), which are probably due to measurement errors and differences in RV dispersion and binary fraction. However, we included them in our analysis because this cluster, as well as the other ones, does not contain many stars and suffers from low number statistics. Therefore, from their RVs, we derived a mean cluster RV of 56.37 ± 2.78 km s^{-1} (Table 4). We used this kinematic and distance information to reconstruct the orbit of ESO 92-18 for the first time. Figure B.1a shows the computed orbits projected on the equatorial and meridional Galactic planes in the inertial reference frame. ESO 92-18 is found to have a low eccentricity ($e \approx 0.09$) and a prograde orbital configuration (see Table 5), with perigalactocentric and apogalactocentric distances inside the Galactic disk of 8.7 kpc and 12 kpc, and vertical excursions from the Galactic plane $|Z|_{\mathrm{max}} \lesssim 1.4$ kpc.

3.4. Ferrero 54

Garro et al. (2022a) found Ferrero 54 behind a nebulosity of dust and gas, which are part of the Vela supernova remnant complex. These authors classified Ferrero 54 as one of the most metal-rich GCs in the MW, with an age of ≈11 Gyr and a metallicity of [Fe/H] = −0.2 ± 0.2. We investigated Ferrero 54 using a combination of the optical *Gaia* DR3 and the NIR VVV/VVVX dataset. Consequently, as derived by this latter work and by the present one, we find that Ferrero 54 is situated at 7.2 kpc from the Sun and 11.6 kpc from the Galactic centre. We also searched for giant stars with RVs in the *Gaia* DR3 catalogue, but find only one target for this cluster (ID_{Gaia} = 5522814131438395904), which appears to be a member because it is located at ∼0.7′ from the cluster centre and its PMs matches the mean cluster PM. Therefore, we adopted the RV of this star as the cluster RV, 56.06 ± 3.17 km s^{-1} (Table 4). Reconstructing the orbits, as described in Sect. 3.2, we find a moderately low eccentricity ($e \approx 0.32$) and a prograde orbital configuration. As displayed in Fig. B.1b and specified in Table 5, its perigalactocentric and apogalactocentric distances are 7 kpc and 13.7 kpc,

Table 4. Kinematical properties of the new GCs from the *Gaia* DR3 catalogue.

ID_{Gaia}	RA [hh:mm:ss]	Dec [dd:mm:ss]	μ_{α_*} [mas yr^{-1}]	μ_δ [mas yr^{-1}]	G [mag]	RV [km s^{-1}]	$\mathrm{err}_{\mathrm{RV}}$ [km s^{-1}]
Patchick 126							
5962848851052186496	17:05:38.56	−47:20:31.1	−4.922	−6.601	14.801	−124.24	1.94
5962848855374108416	17:05:38.59	−47:20:18.5	−4.888	−6.483	15.131	−122.48	1.99
5962848855374110464	17:05:37.42	−47:20:24.2	−4.783	−6.743	15.758	−123.96	4.64
mean ± error						−123.56	2.86
Patchick 125							
5977223075796635392	17:05:03.54	−35:29:13.2	−3.905	0.720	14.646	99.77	2.85
5977220056455257856	17:05:09.69	−35:30:39.8	−3.743	0.700	14.931	93.76	4.55
5977222977074596992	17:05:04.01	−35:31:07.8	−4.338	0.307	15.360	93.87	4.92
5977223316333009024	17:04:58.14	−35:28:36.1	−3.496	0.784	14.585	92.19	2.25
5977223148873371520	17:04:56.53	−35:30:17.3	−3.572	0.128	15.218	89.80	5.45
5977223217592886912	17:04:53.95	−35:29:48.2	−3.859	0.701	14.170	89.23	1.86
mean ± error						93.10	3.65
Patchick 122							
5309623465377355904	09:42:24.24	−52:26:12.8	−3.703	3.756	16.114	97.95	4.16
5309623740255282560	09:42:43.01	−52:24:28.6	−3.709	3.942	15.240	99.41	2.71
mean ± error						98.68	3.43
Kronberger 99							
5327541519172838912	09:11:20.78	−46:22:50.5	−3.667	4.496	14.942	58.00	2.02
5327541175575448576	09:11:14.72	−46:23:15.2	−3.626	4.431	15.912	60.79	4.24
mean ± error						59.39	3.13
Kronberger 119							
5241408114747327616	10:47:27.72	−63:19:41.5	−3.897	1.802	15.093	93.55	3.50
5241409660935539968	10:47:20.02	−63:18:35.6	−3.818	1.735	15.182	97.80	3.65
5241408767582395264	10:47:00.30	−63:20:32.6	−3.880	2.372	15.420	111.60	12.95
5241409592216066560	10:47:23.67	−63:18:56.6	−3.900	1.756	15.494	111.66	7.19
mean ± error						103.65	6.8
Kronberger 143							
5332875215764031360	11:57:43.72	−64:10:16.9	−7.621	0.847	14.718	17.83	1.58
5332875215764037248	11:57:40.96	−64:10:00.9	−7.629	0.786	15.828	16.52	6.69
5332875215764041472	11:57:41.12	−64:09:53.2	−7.761	0.623	15.302	19.55	3.30
mean ± error						17.97	3.86
ESO 92-18							
5252334438496787968	10:14:56.58	−64:36:41.5	−3.657	2.745	13.670	54.34	1.71
5252334404137020544	10:14:56.31	−64:37:20.0	−3.542	2.791	14.963	62.64	4.18
5252335198729523968	10:14:49.51	−64:35:57.3	−3.525	2.734	14.367	51.98	2.68
5252332930986762624	10:14:50.02	−64:37:42.0	−3.427	2.983	12.998	55.45	0.85
5252334511534802432	10:15:12.03	−64:35:45.4	−3.604	2.700	15.145	57.42	4.49
mean ± error						56.37	2.78
ESO 93-08							
5237100842334188032	11:21:12.40	−65:17:05.6	−3.681	1.649	14.400	125.94	1.14
5237115621348452480	11:19:29.25	−65:12:37.9	−4.078	1.359	15.054	128.86	3.38
5237092084927340160	11:21:25.86	−65:29:55.6	−4.423	1.519	14.764	129.55	2.23
mean ± error						128.12	2.25
Gaia 2							
407784471626466304	01:52:22.19	+53:02:32.7	−1.477	1.215	15.033	−52.81	5.96
407784501689316096	01:52:20.94	+53:03:15.7	−1.309	1.173	13.680	−55.89	1.56
mean ± error						−54.36	3.76
Ferrero 54							
5522814131438395904	08:33:45.13	−44:27:00.8	−1.334	1.190	15.518	56.05	3.17
mean ± error						56.05	3.17

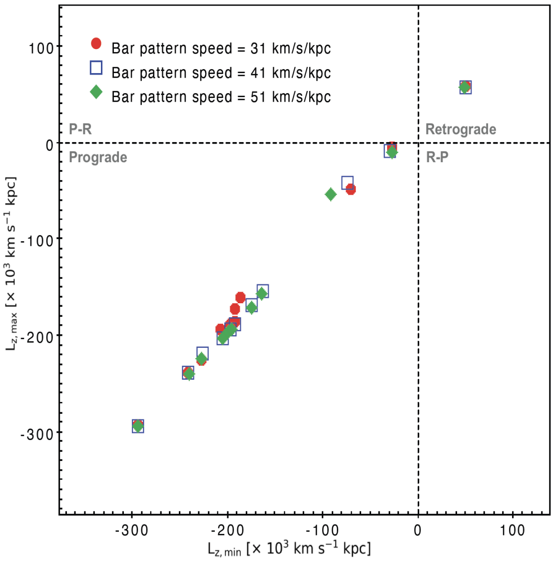

Fig. 5. Minimum and maximum value of the Z-component of the angular momentum (L_z) for our sample clusters in the inertial frame. Black dashed lines split the regions dominated by prograde and retrograde orbits, and those that have prograde and retrograde (P-R) or retrograde and prograde (R-P) orbits at the same time. All star clusters in our sample show prograde orbits, except Patchick 125, which has a retrograde orbit.

respectively. Therefore, Ferrero 54 is moving around the Galactic disk, with vertical excursions from the Galactic plane $|Z|_{\max} \lesssim 0.6$ kpc.

3.5. Gaia 2

Gaia 2, studied by Garro et al. (2022a), is one of the faintest GCs in our sample (along with Patchick 125). It is difficult to study because it is also poorly populated, especially along the evolved sequences in the CMD. However, it does exhibit a well-defined main sequence turn-off and upper part of the main sequence, which helped us to better estimate the age of this cluster. Indeed, we classify it as a GC with an age = 10 ± 1 Gyr, and a metallicity of [Fe/H] = −0.9 ± 0.2. Re-analysing it with the *Gaia* DR3 and VVVX data, we derive a heliocentric distance of 4.7 kpc and Galactocentric distance of 11.9 kpc (Table 1), in agreement with Garro et al. (2022a). In this case, we obtain a mean cluster RV of -54.4 ± 3.8 km s^{-1} (Table 4) using the kinematic information coming from two stars considered members of the cluster because they are located at $r \lesssim 3.1'$ from the centre coordinates, and their PMs coincide with the cluster PM. Furthermore, we reconstructed the orbits for this cluster, finding a very low eccentricity ($e \approx 0.09$) and a prograde motion (Fig. B.1c). Our observations caught *Gaia* 2 very close to the pericentre of its orbit, which is $r_{\rm peri} = 11.5$ kpc, while we calculated an apogalactocentric distance of 13.6 kpc. Its vertical excursions are $|Z|_{\max} \lesssim 1.69$ kpc from the Galactic plane.

3.6. Kronberger 99

The classification of this cluster as a bona fide GC was questioned by Garro et al. (2022a), as Kronberger 99 is a sparsely populated cluster and its CMD does not even reach the main sequence turn-off; estimating a robust age for this cluster was a challenging task. Again, we adopted the *Gaia* DR3 dataset to analyse Kronberger 99. We find an old OC or young GC with an age of >6 Gyr, a metallicity of [Fe/H] = −0.8 ± 0.2, a location at $D_\odot = 4.1$ kpc, and a Galactocentric distance of $R_G = 9.26$ kpc. Additionally, two members whose positions and PMs match those of the cluster were selected, deriving a mean cluster RV of 59.39 ± 3.13 km s^{-1} (Table 4). For Kronberger 99, we derived a low eccentricity ($e \approx 0.1$) and a prograde orbital configuration, with perigalactocentric and apogalactocentric distances of 7.4 kpc and 9.6 kpc, respectively, and vertical excursions from the Galactic plane of 0.34 kpc, as listed in Table 5 and shown in Fig. B.1d. Therefore, we observe Kronberger 99 near to the apocentre of its orbits.

3.7. Kronberger 119

Kronberger 119 was classified as a young GC or an old OC with an age of 6 ± 1 Gyr and a metallicity of [Fe/H] = −0.5 ± 0.2 by Garro et al. (2022a). We confirm the results of these authors after comparing them with the *Gaia* DR3 catalogue. Moreover, we find this cluster at a heliocentric distance of 10.6 kpc and 11.0 kpc from the Galactic centre. We identified four stars belonging to Kronberger 119 with reliable RVs, which give a mean cluster RV of 103.6 ± 6.8 km s^{-1} (Table 4). Although the uncertainties on the *Gaia* RVs are relatively high, in this case the high uncertainty is mostly due to the star ID$_{Gaia}$ =5241408767582395264, which has a large RV error.

After obtaining robust kinematic and distance estimates, we modelled the orbits for this cluster, deriving a moderately low eccentricity ($e \approx 0.3$) and a prograde orbital configuration, as detailed in Table 5. We observed Kronberger 119 at the apocentre of its orbits, or very close, at $r_{\rm apo} = 11.05{-}11.65$ kpc, depending on the bar speed configuration. We find a perigalactocentric distance of $r_{\rm peri} \lesssim 6.35$ kpc. Its vertical excursions are $|Z|_{\max} \approx 0.95$ kpc from the Galactic plane, as shown in Fig. B.1e.

3.8. Kronberger 143

We inspected Kronberger 143 using a matching catalogue of the optical *Gaia* DR3 and the NIR VVVX datasets. As in Garro et al. (2022a), we classify this object as an old OC or a young GC with an age of 6 ± 1 Gyr and a metallicity of [Fe/H] = −0.6 ± 0.2. We place this cluster at a mean distance of 6.4 kpc from the Sun, and 7.77 kpc from the MW centre (Table 1). We selected three star members with *Gaia* RVs for this cluster, which provide a low mean cluster RV of 17.97 ± 3.86 km s^{-1} (Table 4). Computing the orbits for Kronberger 143, as described in Sect. 3.2, we obtain a low eccentricity ($e \approx 0.13$) with prograde orbital configuration. During its travel, it can reach distances of between $r_{\rm peri} = 6.5$ kpc and $r_{\rm apo} < 8.0$ kpc, depending on the bar pattern speed assumed. Vertical excursions of $|Z|_{\max} \approx 0.4$ kpc from the Galactic plane are obtained (Table 5). The most probable orbits are displayed in Fig. B.1f.

3.9. Patchick 122

This is another poorly populated (about 28 stars are found in the magnitude range of $8 < K_s < 16$) and small GC candidate. Using both the *Gaia* EDR3 (Garro et al. 2022a) and DR3 datasets, we derive an age of 10 Gyr (with a lower limit of 6 Gyr) and [Fe/H] = −0.5 ± 0.2. We place Patchick 122 at a heliocentric distance of $D_\odot = 5.1$ kpc and a Galactocentric distance of $R_G = 9.2$ kpc. The RV information is derived from two member stars, from which we calculated a mean cluster RV of 98.7 ± 3.4 km s^{-1}. With these kinematic and distance values (Table 1), we obtained low eccentricity ($e \approx 0.23$) and prograde orbits, with perigalactocentric and apogalactocentric distances of 5.1 kpc and 9.8 kpc, respectively. Vertical excursions of $|Z|_{\max} \approx 0.24$ kpc from the Galactic plane were obtained; see Table 5 and Fig. B.1g. We observed Patchick 122 near to the apocentre of its orbits.

3.10. Patchick 125

This GC candidate was photometrically analysed by Garro et al. (2022a) using a combination of the *Gaia* EDR3 and VVVX datasets. Investigating this cluster by adopting the *Gaia* DR3 and VVVX catalogue, we obtain similar results. Therefore, we confirm that Patchick 125 is a metal-poor ([Fe/H] $\sim -1.8 \pm 0.2$) and old (age = 13−14 Gyr) GC. Furthermore, as done by Garro et al. (2022a), we identified the same two RR Lyrae stars in the updated *Gaia* catalogue with ID_{Gaia} = 5977224553266268928 and ID_{Gaia} = 5977223144516980608, and derived the cluster distance using an independent method. We obtain similar results to Garro et al. (2022a): a distance of 10.4 kpc for 5977224553266268928, and a distance of 11.5 kpc for 5977223144516980608. We estimated the heliocentric distance both from an RR Lyrae period–luminosity–metallicity relation and in the NIR and optical wavelengths. In this manner, we derive a mean heliocentric distance of $D_\odot$ = 11.1 kpc, which places this cluster at a Galactocentric distance of R_G = 3.4 kpc. From the *Gaia* DR3 catalogue, we identified six cluster star members with similar RVs, as specified in Table 4. This provides a mean cluster RV of $93.1 \pm 3.6\,\mathrm{km\,s^{-1}}$, in good agreement with the values found by Fernández-Trincado et al. 2022 (RV = $95.9\,\mathrm{km\,s^{-1}}$)) derived from the APOGEE-2S data. These RV values are not in perfect agreement with the value reported by Gran et al. (2022) of $74.23\,\mathrm{km\,s^{-1}}$. Using our mean RV, distances, and PMs, we reconstructed the orbits of Patchick 125, obtaining a moderately low eccentricity ($e \approx 0.3$) and a retrograde orbital configuration (Fig. B.1h). It moves between r_peri = 2.3 kpc and r_apo = 4.5 kpc, therefore straddling the edge of the bulge ($R_G \approx 3 - 3.5$ kpc) and the halo of the MW. Additionally, its vertical excursion is $|Z|_\mathrm{max} \approx 3.3$ kpc from the Galactic plane (Table 5).

3.11. Patchick 126

As described in Sect. 2.1, we observed Patchick 126 with the IGRINS spectrograph (Table 2). We were therefore able to inspect this cluster both from a photometric and a spectroscopic point of view. Photometrically, Patchick 126 was first analysed by Garro et al. (2022a), who found it to be a young bulge GC. We confirm their results, as we estimate an age of $\gtrsim$8 Gyr and a metallicity of [Fe/H] = -0.7 ± 0.3. Its heliocentric distance is 8.0 kpc, while its Galactocentric distance is 2.8 kpc. The kinematic information for Patchick 126 derived from the IGRINS spectroscopic data is $\mathrm{RV}^{H,K}_\mathrm{IGRINS} = -121.8 \pm 0.25\,\mathrm{km\,s^{-1}}$, which is in perfect agreement with the *Gaia* DR3 *RV* = $-123.56 \pm 2.86\,\mathrm{km\,s^{-1}}$ obtained from three cluster stars (Table 4). We adopt the IGRINS RVs because their uncertainties were smaller than the *Gaia* ones. We derive a moderately low eccentricity ($e \approx 0.35$) and prograde orbits. Patchick 125, as in Patchick 126, moves in the corner of the Galactic bulge, sinking to r_peri = 1.6 kpc and reaching a larger distance at r_apo = 4.2 kpc, depending on the bar pattern speed (Table 5). The vertical excursion from the Galactic plane is 0.65 kpc, as shown in Fig. B.1i. We caught this GC inside the MW bulge.

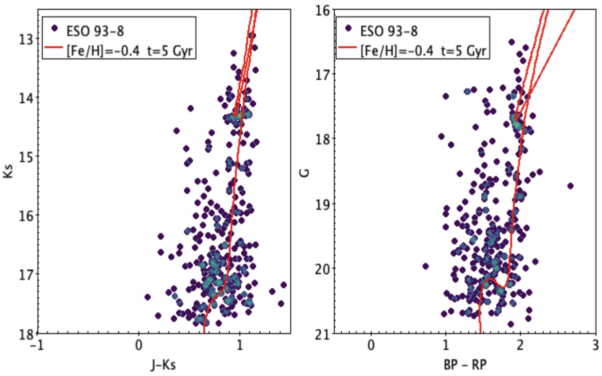

Fig. 6. VVVX (*left panel*) and *Gaia* DR3 (*right panel*) CMD of ESO 93-08. We used the PARSEC v3.7 isochrone model (Bressan et al. 2012; Marigo et al. 2013). The best isochrone fit yields an age of 5 Gyr and a metallicity of [Fe/H] = −0.4.

3.12. ESO 93-08

ESO 93-08 is a poorly studied star cluster classified as a GC candidate. It was previously catalogued with the names of ESO 093-SC08 and GCL B1117-6456. First analysed by Bica et al. (1999), these authors found an age of 4–5 Gyr by comparison of the magnitude difference between the main sequence turn-off and the red clump, along with a reddening $E(B-V)$ = 0.64, and a distance modulus $(m-M)_0$ of 15.68 ± 0.2 mag, corresponding to a heliocentric distance of 13.5 ± 0.6 kpc. Subsequently, Phelps & Schick (2003) confirmed the Bica et al. values, and also found a distance modulus of 15.75 mag, equivalent to a heliocentric distance of 14.0 ± 0.7 kpc, an age of 5.5 ± 1.0 Gyr, and a metallicity of [Fe/H] = -0.4 ± 0.2. Furthermore, their Galactocentric position ($R_G = 13.0 \pm 0.7$) placed ESO 93-08 in the outer disk, with a high vertical displacement from the disk ($Z = -1000 \pm 50$ pc).

We analysed this star cluster using a combination of the optical *Gaia* DR3 and the NIR VVVX datasets. We performed our decontamination procedure following Garro et al. (2022a,b), adopting a mean cluster PM of $\mu_{\alpha_*} = -4.07 \pm 0.03\,\mathrm{mas\,yr^{-1}}$ and $\mu_\delta = 1.40 \pm 0.03\,\mathrm{mas\,yr^{-1}}$, in agreement with Vasiliev & Baumgardt (2021). With the clean CMDs for both the VVVX and *Gaia* passbands (Fig. 6), we derived its main physical parameters. The reddening and extinction in the NIR are $E(J-K_s) = 0.39 \pm 0.01$ mag and $A_{Ks} = 0.29 \pm 0.01$ mag, respectively, while in the optical they are $E(BP-RP) = 0.85 \pm 0.01$ mag and $A_G = 1.7 \pm 0.01$ mag, respectively. We also obtained a distance modulus of 15.66 ± 0.02 mag, corresponding to $D_\odot = 13.6 \pm 1.0$ kpc, which places ESO 93-08 at R_G = 12.8 kpc. Adopting the isochrone-fitting method, we photometrically estimated an age of >5 Gyr and a metallicity of -0.4 ± 0.2. All the estimated parameters are in good agreement with those found by Phelps & Schick (2003).

As was done for the other cluster candidates in our sample, we searched for star-cluster members with suitable RVs in the *Gaia* DR3 catalogue. We find three stars with similar RVs, as listed in Table 4. However, even if their PMs (as well as the RVs) match the mean cluster PMs, we further investigated two stars, named ID_{Gaia} = 5237100842334188032 and ID_{Gaia} = 5237092084927340160, because they are located at $r > 6'$ from the ESO 93-08 centre. Therefore, we reconstructed the orbits for this cluster using the mean cluster RV of 128.12 ± 2.25, finding a moderately low eccentricity ($e \approx 0.33$) and prograde orbital configuration. Its perigalactocentric distance is ~6.0 kpc, and its apogalactocentric distance is 12.1 kpc, while its vertical excursions are 1.15 kpc, depending on the assumed bar patter speed. Additionally, we ran the GravPot16 algorithm for only ID_{Gaia} = 5237115621348452480 and obtained very similar results, which do not modify the final conclusion for this cluster.

3.13. VVV-CL160

First classified as an old metal-poor open cluster by Borissova et al. (2014), VVV-CL160 was subsequently analysed by Minniti et al. (2021) and reclassified as a metal-poor GC with an age of 12 Gyr and a metallicity of [Fe/H] $= -1.4$, located at 4.0 kpc from the Sun. Intriguingly, Minniti et al. (2021) concluded that VVV-CL160 may belong to a disrupted dwarf galaxy, because the kinematics are similar to those of the GC NGC 6544 and the Hrid halo stream. Later, Garro et al. (2022b) confirmed its GC nature, as they found a metallicity of -1.4 ± 0.3 and an age of 13 ± 2 Gyr. However, these authors placed this cluster at a greater distance ($D_\odot = 6.8$ kpc, $R_G = 1.92$ kpc).

In the present work, we analysed VVV-CL160 again using only the NIR VVVX catalogue. This is because it is very reddened and *Gaia* is not able to overcome the large extinction. As listed in Table 1, we obtain the same results as Garro et al. (2022b). Additionally, as described in Sect. 2.1, we observed 12 high-likelihood member stars with the high-resolution IGRINS spectrograph during the program GS-2022A-Q-132 (see Table 2). In Sect. 2.3, we explain how we derived the RV for each star, finding robust results in both the H- and K-bands (see Table 3). Calculating the mean of these RV values, we obtained the mean cluster RV in both bands, $\mathrm{RV}_H = 245.57 \pm 0.58\,\mathrm{km\,s^{-1}}$ and $\mathrm{RV}_K = 245.03 \pm 0.56$. We used their mean value in order to reconstruct the orbits for VVV-CL160 for the first time. We derive a very high eccentricity orbit with $e \approx 0.96$, revealing it as a cluster with among the most eccentric orbits known among the Galactic GCs (Vasiliev & Baumgardt 2021). Moreover, its orbital configuration is prograde, with a perigalactocentric distance of 0.2 kpc and apogalactocentric distance of 10.5 kpc, and vertical excursions of 3.5 kpc. Indeed, as shown in Fig. B.1k, VVV-CL160 barges into the innermost MW bulge regions, passing very close to the Galactic centre, and reaches very large distances beyond the Sun's orbit. Finally, both the kinematic and dynamic information allowed us to rule out its membership of the Hrid stream.

4. Discussion

Various works have classified star clusters, and in particular GCs, based on their dynamical properties. Here, we took into account the work of Massari et al. (2019). These authors find that young and metal-rich GCs typically do not reach high $Z_{\max}$, and that they have smaller apocentres and tend to have lower eccentricities. Also, as indicated by Leaman et al. (2013), these young and metal-rich GCs are in situ clusters, formed in the Galactic bulge or disk. Therefore, Leaman et al. (2013) classified as bulge clusters those GCs with bound orbits and $r_{\mathrm{apo}} < 3.5$ kpc (e.g., HP 1, Terzan 1, NGC 6380, NGC 6440), while classifying disk clusters as those GCs with $Z_{\max} < 5$ kpc and circularity[8] $circ > 0.5$ (e.g., NGC 104, Pal 1, NGC 6569, FSR 1716). Massari et al. (2019) referred to them as the main progenitor. Additionally, these latter authors recognised some old metal-poor GCs with similar orbits to young metal-rich GCs, and therefore included them as the main progenitor. On the other hand, Massari et al. (2019) also recognised the accreted clusters, indicating their progenitors: Sagittarius dwarf galaxy with $0 < L_Z < 3000\,\mathrm{km\,s^{-1}}$, Helmi streams with $350 < L_Z < 3000\,\mathrm{km\,s^{-1}}$, Gaia-Enceladus with $-800 < L_Z < 620\,\mathrm{km\,s^{-1}}$, and Sequoia with $-3700 < L_Z < -850\,\mathrm{km\,s^{-1}}$ (we refer to Massari et al. 2019 for more details).

At this point, based on the Massari et al. (2019) analysis, we can classify the clusters of our sample as having formed in situ, and therefore they are part of the main progenitor, apart from the GC VVV-CL160. In particular, Patchick 125 and Patchick 126 are genuine MW bulge/halo GCs, because their r_{apo} are <4.2 kpc and <4.5 kpc, respectively, adopting $\Omega_{\mathrm{bar}} = 51\,\mathrm{km\,s^{-1}\,kpc^{-1}}$. Even if their L_Z could also match the values of the *Gaia*-Enceladus accretion event, we exclude their membership because the *Gaia*-Enceladus stars have: larger apogalactic distances; $r_{\mathrm{apo}} < 25$ kpc (Deason et al. 2018), mean metallicity of [Fe/H] ~ -1.15, and a mean age of 10–12 Gyr (Feuillet et al. 2021), which are different from our estimates for the cluster candidates studied here (Table 1). Furthermore, we find that the majority of the objects of our sample exhibit disk-like orbits. However, we can split the sample into disk GCs, including Ferrero 54, *Gaia* 2, and Patchick 122, and disk old open clusters, including Kronberger 99, Kronberger 119, Kronberger 143, ESO 92-18, and ESO 93-08. All clusters in our sample show prograde orbits, except for Patchick 125 (Fig. 5). Obreja et al. (2022) suggested that the excess of prograde clusters may be connected to the motion of the Galactic halo itself – which initially could contain prograde clusters – or to the spinning of the dark matter halo.

On the other hand, the history of VVV-CL160 could be different from that of the other clusters in our sample. Its orbit is very eccentric, and it moves from the innermost regions to larger distances beyond the Sun. Such orbits suggest that VVV-CL160 was sufficiently massive to survive strong dynamical effects (e.g., dynamical friction) typical of the inner regions. Although we exclude its membership of the Hrid stream, as explained in Sect. 3.13, we cannot rule out the possibility that this GC was formed outside our Galaxy, and only subsequently accreted into the MW after a merger event. Instead, if we suppose that VVV-CL160 formed in situ, we could explain its very eccentric orbit as the result of an encounter between the MW and another galaxy, which may have changed the orbit of this GC. Simulations are needed to further explore this hypothesis.

5. Concluding remarks

The main goal of the present paper is to reconstruct the orbits of 11 star clusters for the first time, taking advantage of the precise astrometry, proper motions, and RVs of the *Gaia* DR3 dataset. We first photometrically analysed these clusters (see Table 1) using a combination of the optical *Gaia* DR3 and the NIR VVVX data, finding similar results to previous works (Garro et al. 2022a,b). Subsequently, we derived the RVs for 12 star-cluster members in VVV-CL160 and four in Patchick 126 using the high-resolution IGRINS spectrograph. These stars were observed during Programs `GS-2022A-Q-132` and `GS-2022A-Q-238` (PI: Garro E.R. – Table 2), respectively. Notably, we found similar results in both the H- and K-bands for the two clusters, as seen in Table 3. Additionally, similar agreement is found for the RVs obtained from IGRINS spectra and *Gaia* DR3 data for Patchick 126, even if the *Gaia* RV errors are larger than the IGRINS ones, as expected. For the other clusters in our sample, we obtained suitable RVs, after having carefully selecting stars in each target based on their proper motions, distances from the cluster centre, and similar RVs. The stars that were selected are listed in Table 4. However, we did not detect good VVV-CL160 stars in the *Gaia* DR3 dataset, because this cluster is very reddened and inaccessible to *Gaia*.

---

[8] As specified by Massari et al. (2019), orbital circularity is $circ = L_Z/L_{Z,\mathrm{circ}}$, where $L_{Z,\mathrm{circ}}$ is the angular momentum of a circular orbit with the cluster energy, which thus takes extreme values +1 or −1 for co-planar circular prograde or retrograde orbits, respectively.

Table 5. Orbital elements for each stellar cluster at different bar pattern speeds.

Cluster	$r_{\rm peri}$ [kpc]	$r_{\rm apo}$ [kpc]	Eccentricity	$Z_{\rm max}$ [kpc]	$L_{z\rm min}$ [$\times 10^3$ km s^{-1} kpc]	$L_{z\rm max}$ [$\times 10^3$ km s^{-1} kpc]
$\Omega_{\rm bar} = 31$ km s^{-1} kpc^{-1}						
Patchick 126	1.87 ± 0.75	3.78 ± 0.23	0.33 ± 0.18	0.61 ± 0.11	−71.0 ± 7.0	−48.0 ± 12.5
VVV-CL160	0.17 ± 0.20	10.49 ± 3.04	0.97 ± 0.04	3.26 ± 1.75	−28.0 ± 11.5	−5.0 ± 15.5
Ferrero 54	7.04 ± 0.70	13.72 ± 1.21	0.32 ± 0.04	0.63 ± 0.47	−228.0 ± 17.5	−225.0 ± 18.0
Gaia 2	11.52± 0.83	13.55 ± 2.19	0.09 ± 0.05	1.69 ± 0.64	−294.0 ± 29.5	−292.0 ± 29.5
ESO 92-18	8.75 ± 1.54	11.93 ± 1.31	0.16 ± 0.05	1.4 ± 0.26	−242.0 ± 31.5	−239.0 ± 33.0
Kronberger 143	6.59 ± 0.60	8.69 ± 0.79	0.14 ± 0.03	0.44 ± 0.24	−193.0 ± 18.0	−172.0 ± 12.5
Kronberger 119	6.09 ± 1.86	11.06 ± 0.64	0.29 ± 0.12	0.95 ± 0.39	−197.0 ± 30.0	−188.0 ± 40.5
Kronberger 99	7.37 ± 1.48	9.41 ± 0.30	0.13 ± 0.08	0.34 ± 0.15	−208.0 ± 15.0	−193.0 ± 29.0
Patchick 125	2.34 ± 0.63	4.04 ± 1.22	0.28 ± 0.10	3.05 ± 1.09	50.0 ± 17.0	59.0 ± 12.0
Patchick 122	5.24 ± 0.68	9.81 ± 0.75	0.32 ± 0.04	0.24 ± 0.22	−187.0 ± 20.0	−160.0 ± 14.5
ESO 93-08	5.87 ± 1.94	11.52 ± 0.75	0.33 ± 0.12	1.11 ± 0.43	−193.0 ± 36.6	−186.0 ± 45.6
$\Omega_{\rm bar} = 41$ km s^{-1} kpc^{-1}						
Patchick 126	1.56 ± 0.36	3.87 ± 0.26	0.42 ± 0.11	0.72 ± 0.11	−74.0 ± 9.5	−41.0 ± 6.5
VVV-CL160	0.21 ± 0.21	10.63 ± 2.76	0.97 ± 0.04	3.54 ± 1.77	−30.0 ± 11.5	−8.0 ± 12.0
Ferrero 54	7.03 ± 0.69	13.68 ± 0.93	0.32 ± 0.05	0.62 ± 0.44	−227.0 ± 15.0	−218.0 ± 18.6
Gaia 2	11.55 ± 0.84	13.59 ± 2.16	0.09 ± 0.04	1.69 ± 0.63	−294.0 ± 29.5	−294.0 ± 29.5
ESO 92-18	8.79 ± 1.55	12.16 ± 1.08	0.16 ± 0.06	1.42 ± 0.25	−242.0 ± 29.5	−238.0 ± 32.0
Kronberger 143	6.41 ± 1.57	7.92 ± 0.87	0.13 ± 0.09	0.42 ± 0.24	−175.0 ± 20.0	−168.0 ± 41.5
Kronberger 119	6.34 ± 1.63	11.08 ± 0.83	0.27 ± 0.09	0.95 ± 0.41	−197.0 ± 32.5	−193.0 ± 34.5
Kronberger 99	7.76 ± 1.21	9.28 ± 0.67	0.10 ± 0.04	0.33 ± 0.16	−206.0 ± 23.0	−203.0 ± 24.0
Patchick 125	2.30 ± 0.70	4.13 ± 1.36	0.30 ± 0.13	3.28 ± 1.18	50.0 ± 18.5	58.0 ± 13.5
Patchick 122	5.06 ± 1.65	9.13 ± 0.51	0.29 ± 0.14	0.23 ± 0.21	−163.0 ± 21.0	−154.0 ± 45.0
ESO 93-08	6.00 ± 1.73	11.55 ± 1.01	0.32 ± 0.09	1.12 ± 0.43	−193.0 ± 38.1	−188.0 ± 40.1
$\Omega_{\rm bar} = 51$ km s^{-1} kpc^{-1}						
Patchick 126	2.26 ± 0.51	4.20 ± 0.51	0.32 ± 0.09	0.63 ± 0.11	−92.0 ± 12.0	−53.0 ± 9.0
VVV-CL160	0.25 ± 0.20	10.54 ± 3.17	0.96 ± 0.03	3.55 ± 1.50	−28.0 ± 11.5	−10.0 ± 10.0
Ferrero 54	7.02 ± 0.71	13.74 ± 1.39	0.32 ± 0.05	0.63 ± 0.45	−228.0 ± 18.0	−224.0 ± 16.5
Gaia 2	11.55 ± 0.86	13.59 ± 2.15	0.08 ± 0.04	1.69 ± 0.63	−294.0 ± 29.5	−294.0 ± 29.5
ESO 92-18	8.81 ± 1.53	11.82 ± 1.24	0.15 ± 0.05	1.40 ± 0.26	−241.0 ± 31.5	−240.0 ± 32.5
Kronberger 143	6.54 ± 0.83	7.96 ± 1.17	0.12 ± 0.04	0.43 ± 0.25	−175.0 ± 21.0	−171.0 ± 23.5
Kronberger 119	6.35 ± 1.61	11.65 ± 0.51	0.29 ± 0.11	0.99 ± 0.40	−200.0 ± 27.5	−196.0 ± 37.0
Kronberger 99	7.76 ± 1.40	9.62 ± 0.54	0.10 ± 0.08	0.35 ± 0.16	−206.0 ± 16.5	−203.0 ± 23.5
Patchick 125	2.27 ± 0.63	4.50 ± 1.24	0.31 ± 0.13	3.28 ± 1.13	49.0 ± 17.0	58.0 ± 14.0
Patchick 122	5.15 ± 0.92	9.37 ± 0.75	0.30 ± 0.05	0.23 ± 0.21	−165.0 ± 22.0	−157.0 ± 18.0
ESO 93-08	6.02 ± 1.74	12.12 ± 0.92	0.34 ± 0.11	1.15 ± 0.43	−196.0 ± 36.0	−193.0 ± 44.0

Once distances, mean cluster PMs, and mean cluster RVs were obtained, we reconstructed the orbits for these clusters using the `GravPot16` model. The results are summarised in Table 5 and shown in Fig. B.1. We can conclude that all clusters show prograde orbits, except for Patchick 125, which has a retrograde orbit. Patchick 125 and Patchick 126 are genuine MW GCs, moving on orbits straddling the Galactic bulge and halo. Ferrero 54, *Gaia* 2, and Patchick 122 are disk GCs with disk-like orbits; whereas Kronberger 99, Kronberger 119, Kronberger 143, ESO 92-18, and ESO 93-08 are old open clusters with disk-like orbits. All these star clusters show very low eccentricities, except for VVV-CL160, which exhibits one of the highest known eccentricities ($e \approx 0.97$), indicating that this GC survived only because its initial mass was sufficiently large to be strongly bonded, reducing star loss and allowing it to avoid total destruction.

Finally, we suggest that all star clusters in our sample formed in situ, following the classification by Massari et al. (2019), while we cannot rule out the possibility that VVV-CL160 was accreted into the MW. Clearly, future spectroscopic observations are needed to increase our knowledge about these clusters and other more recently discovered GC candidates in order to derive robust chemical abundances and understand their origin, detect multiple populations (if any), and increase the statistics of the present results. In a subsequent paper, we plan to investigate the chemical abundances for the stars observed in Patchick 126 and VVV-CL160 GCs with the IGRINS spectrograph.

Acknowledgements. We gratefully acknowledge the use of data from the ESO Public Survey program IDs 179.B-2002 and 198.B-2004 taken with the VISTA telescope and data products from the Cambridge Astronomical Survey Unit. This work presents results from the European Space agency (ESA) space mission *Gaia*. *Gaia* data are being processed by the *Gaia* Data Processing and Analysis Consortium (DPAC). Funding for the DPAC is provided by national institutions, in particular the institutions participating in the *Gaia* MultiLateral Agreement (MLA). The *Gaia* mission website is `https://www.cosmos.esa.int/gaia`. The *Gaia* archive website is `https://archives.esac.esa.int/gaia`. This work used the Immersion Grating Infrared Spectrometer (IGRINS) that was developed under a collaboration between the University of Texas at Austin and the Korea Astronomy and Space Science Institute (KASI) with the financial support of the US National Science Foundation 27 under grants AST-1229522 and AST-1702267, of the University of Texas at Austin, and of the Korean GMT Project of KASI. E.R.G. gratefully acknowledges support from ANID PhD scholarship No. 21210330. D.M. gratefully acknowledges support by the ANID BASAL projects ACE210002 and FB210003, and Fondecyt Project No. 1220724. J.G.F-T gratefully acknowledges the grant support provided by Proyecto Fondecyt Iniciación No. 11220340, and also from ANID Concurso de Fomento a la Vinculación Internacional para Instituciones de Investigación Regionales (Modalidad corta duración) Proyecto No. FOVI210020, and from the Joint Committee ESO-Government of Chile 2021 (ORP 023/2021), and from Becas Santander Movilidad Internacional Profesores 2022, Banco Santander Chile. T.C.B. acknowledges partial support for this work from grant PHY 14-30152; Physics Frontier Center/JINA Center for the Evolution of the Elements (JINA-CEE), and OISE-1927130: The International Research Network for Nuclear Astrophysics (IReNA), awarded by the US National Science Foundation. B.D. acknowledges support by ANID-FONDECYT iniciación grant No. 11221366.

References

Barbuy, B., Chiappini, C., & Gerhard, O. 2018, ARA&A, 56, 223
Bica, E., Ortolani, S., & Barbuy, B. 1999, A&AS, 136, 363
Blanco-Cuaresma, S. 2019, MNRAS, 486, 2075
Blanco-Cuaresma, S., Soubiran, C., Heiter, U., & Jofré, P. 2014, A&A, 569, A111
Borissova, J., Chené, A. N., Ramírez Alegría, S., et al. 2014, A&A, 569, A24
Bressan, A., Marigo, P., Girardi, L., et al. 2012, MNRAS, 427, 127
Brunthaler, A., Reid, M. J., Menten, K. M., et al. 2011, Astron. Nachr., 332, 461
Chen, Y., & Gnedin, O. Y. 2022, MNRAS, 514, 4736
Cole, S., Lacey, C. G., Baugh, C. M., & Frenk, C. S. 2000, MNRAS, 319, 168
Deason, A. J., Belokurov, V., Koposov, S. E., & Lancaster, L. 2018, ApJ, 862, L1
Dotter, A., Sarajedini, A., Anderson, J., et al. 2010, ApJ, 708, 698
Fehlberg, E. 1969, Low-order Classical Runge-Kutta Formulas with Stepsize Control and their Application to Some Heat Transfer Problems, 315, (National aeronautics and space administration)
Fernández-Trincado, J. G., Chaves-Velasquez, L., Pérez-Villegas, A., et al. 2020, MNRAS, 495, 4113
Fernández-Trincado, J. G., Minniti, D., Garro, E. R., & Villanova, S. 2022, A&A, 657, A84
Feuillet, D. K., Sahlholdt, C. L., Feltzing, S., & Casagrande, L. 2021, MNRAS, 508, 1489
Forbes, D. A., Bastian, N., Gieles, M., et al. 2018, Proc. Roy. Soc. London Ser. A, 474, 20170616
Frank, M. J., Hilker, M., Baumgardt, H., et al. 2012, MNRAS, 423, 2917
Gaia Collaboration (Prusti, T., et al.) 2016, A&A, 595, A1
Gaia Collaboration (Brown, A. G. A., et al.) 2021, A&A, 649, A1
Gaia Collaboration (Vallenari, A., et al.) 2023, A&A, in press, `https://doi.org/10.1051/0004-6361/202243940`
Garro, E. R., Minniti, D., Gómez, M., et al. 2020, A&A, 642, L19
Garro, E. R., Minniti, D., Gómez, M., et al. 2021, A&A, 649, A86
Garro, E. R., Minniti, D., Alessi, B., et al. 2022a, A&A, 659, A155
Garro, E. R., Minniti, D., Gómez, M., et al. 2022b, A&A, 658, A120
Gonzalez, O. A., Rejkuba, M., Zoccali, M., et al. 2012, A&A, 543, A13
Gran, F., Zoccali, M., Contreras Ramos, R., et al. 2019, A&A, 628, A45
Gran, F., Zoccali, M., Saviane, I., et al. 2022, MNRAS, 509, 4962
Horne, K. 1986, PASP, 98, 609
Katz, D., Sartoretti, P., Guerrier, A., et al. 2023, A&A, in press, `https://doi.org/10.1051/0004-6361/202244220`
Kruijssen, J. M. D., Pelupessy, F. I., Lamers, H. J. G. L. M., Portegies Zwart, S. F., & Icke, V. 2011, MNRAS, 414, 1339
Lallement, R., Vergely, J. L., Babusiaux, C., & Cox, N. L. J. 2022, A&A, 661, A147
Leaman, R., VandenBerg, D. A., & Mendel, J. T. 2013, MNRAS, 436, 122
Lee, J. J., Gullikson, K., & Kaplan, K. 2017, Igrins/Plp 2.2.0 (Zenodo)
Mace, G., Sokal, K., Lee, J. J., et al. 2018, in Ground-based and Airborne Instrumentation for Astronomy VII, eds. C. J. Evans, L. Simard, & H. Takami, SPIE Conf. Ser., 10702, 107020Q
Marigo, P., Bressan, A., Nanni, A., Girardi, L., & Pumo, M. L. 2013, MNRAS, 434, 488
Marigo, P., Girardi, L., Bressan, A., et al. 2017, ApJ, 835, 77
Massari, D., Koppelman, H. H., & Helmi, A. 2019, A&A, 630, L4
Mészáros, S., Prieto, C. A., Edvardsson, B., et al. 2012, AJ, 144, 120
Minniti, D. 1995, AJ, 109, 1663
Minniti, D., Lucas, P. W., Emerson, J. P., et al. 2010, New A, 15, 433
Minniti, D., Geisler, D., Alonso-García, J., et al. 2017, ApJ, 849, L24
Minniti, D., Alonso-García, J., Borissova, J., et al. 2019, Res. Notes AAS, 3, 101
Minniti, D., Fernández-Trincado, J. G., Gómez, M., et al. 2021, A&A, 650, L11
Moreno, E., Fernández-Trincado, J. G., Pérez-Villegas, A., Chaves-Velasquez, L., & Schuster, W. J. 2021, MNRAS, 510, 5945
Obreja, A., Buck, T., & Macciò, A. V. 2022, A&A, 657, A15
Ortolani, S., Bica, E., & Barbuy, B. 2013, MNRAS, 433, 1966
Park, C., Jaffe, D. T., Yuk, I. S., et al. 2014, in IGRINS at the Discovery Channel Telescope and Gemini South, Proc. SPIE, 9147, 1
Parzen, E. 1962, Ann. Math. Stat., 33, 1065
Pérez-Villegas, A., Barbuy, B., Kerber, L. O., et al. 2020, MNRAS, 491, 3251
Pfeffer, J., Kruijssen, J. M. D., Crain, R. A., & Bastian, N. 2017, MNRAS, 475, 4309
Phelps, R. L., & Schick, M. 2003, AJ, 126, 265
Picaud, S., & Robin, A. C. 2004, A&A, 428, 891
Ramos, R. C., Minniti, D., Fernández-Trincado, J. G., et al. 2018, ApJ, 863, 78
Recio-Blanco, A. 2018, A&A, 620, A194
Robertson, B., Bullock, J. S., Font, A. S., Johnston, K. V., & Hernquist, L. 2005, ApJ, 632, 872
Robin, A. C., Reylé, C., Derrière, S., & Picaud, S. 2003, A&A, 409, 523
Robin, A. C., Marshall, D. J., Schultheis, M., & Reylé, C. 2012, A&A, 538, A106
Saito, R. K., Hempel, M., Minniti, D., et al. 2012, A&A, 537, A107
Salaris, M., Weiss, A., & Percival, S. M. 2004, A&A, 414, 163
Sanders, J. L., Smith, L., & Evans, N. W. 2019, MNRAS, 488, 4552
Skrutskie, M. F., Cutri, R. M., Stiening, R., et al. 2006, AJ, 131, 1163
Sneden, C. 1973, ApJ, 184, 839
Sofue, Y. 2015, PASJ, 67, 75
Springel, V., Frenk, C. S., & White, S. D. M. 2006, Nature, 440, 1137
Vasiliev, E., & Baumgardt, H. 2021, MNRAS, 505, 5978
Zucker, S. 2003, MNRAS, 342, 1291

Appendix A: CMDs of analysed clusters

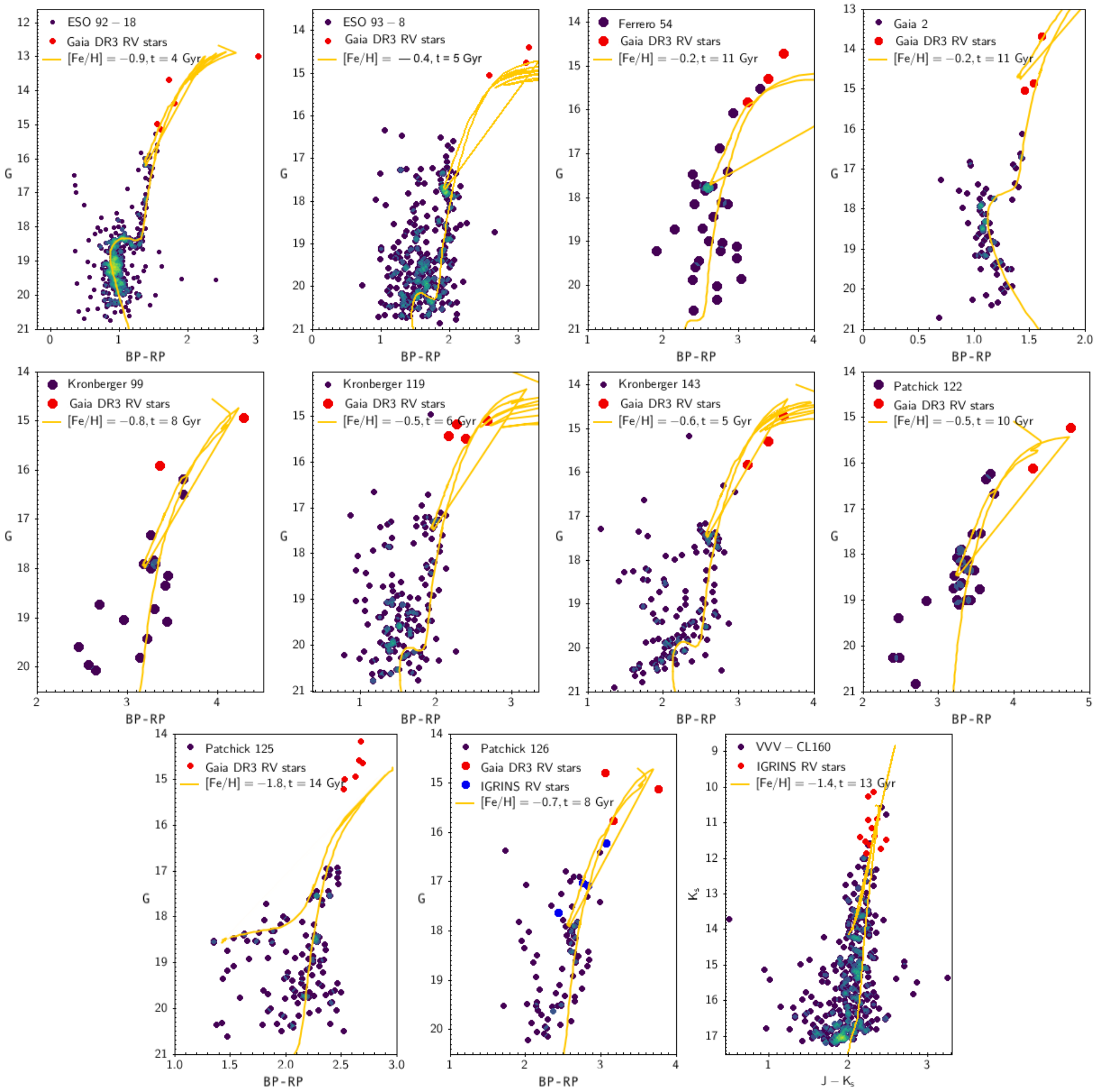

Fig. A.1. Optical CMDs for our targets, while we show the NIR CMD for VVV-CL160. We highlight the stars with reliable *Gaia DR3* (red points) and IGRINS (see in the legend) RVs. The yellow lines represent the Parsec isochrones fit, adopting the age and metallicity as shown in the legend.

Appendix B: Figures of the orbits for the analysed clusters

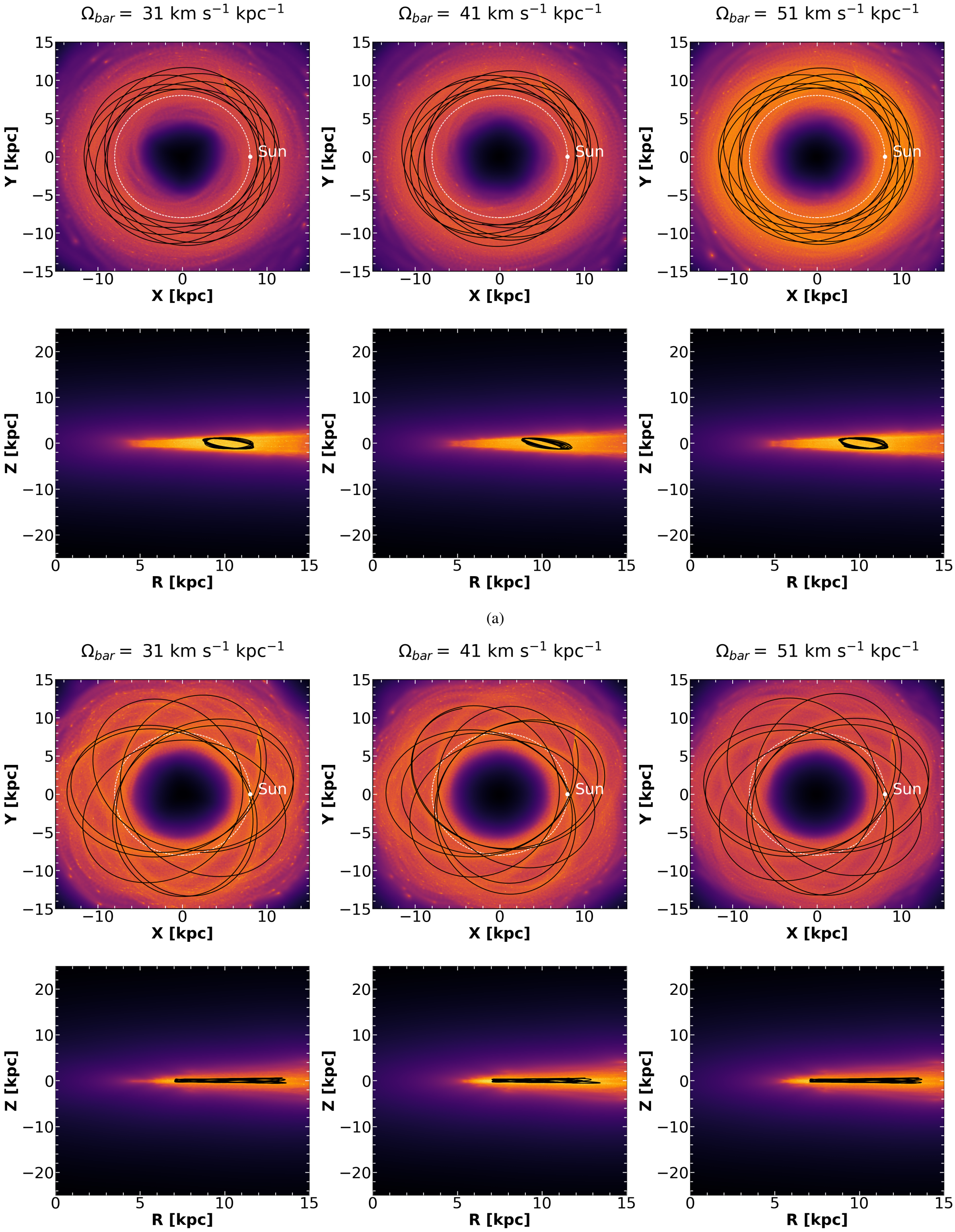

(a)

(b)

Fig. B.1. Orbits. Ensemble of 10 000 orbits for each studied star cluster by considering the errors on the observables, projected on the equatorial (top panels) and meridional (bottom panels) Galactic planes in the inertial reference frame, with a bar pattern speed of 31, 41, and 51 km s^{-1} and integrated over the past 2.0 Gyr. The red and orange colours correspond to more probable regions of the space, which are crossed most frequently by the simulated orbits. The black line shows the orbit of the star cluster from the observables without error bars. (a) ESO 92-18. (b) Ferrero 54. (c) Gaia 2. (d) Kronberger 99. (e) Kronberger 119. (f) Kronberger 143. (g) Patchick 122. (h) Patchick 125. (i) Patchick 126. (j) ESO 98-3. (k) VVV-CL60.

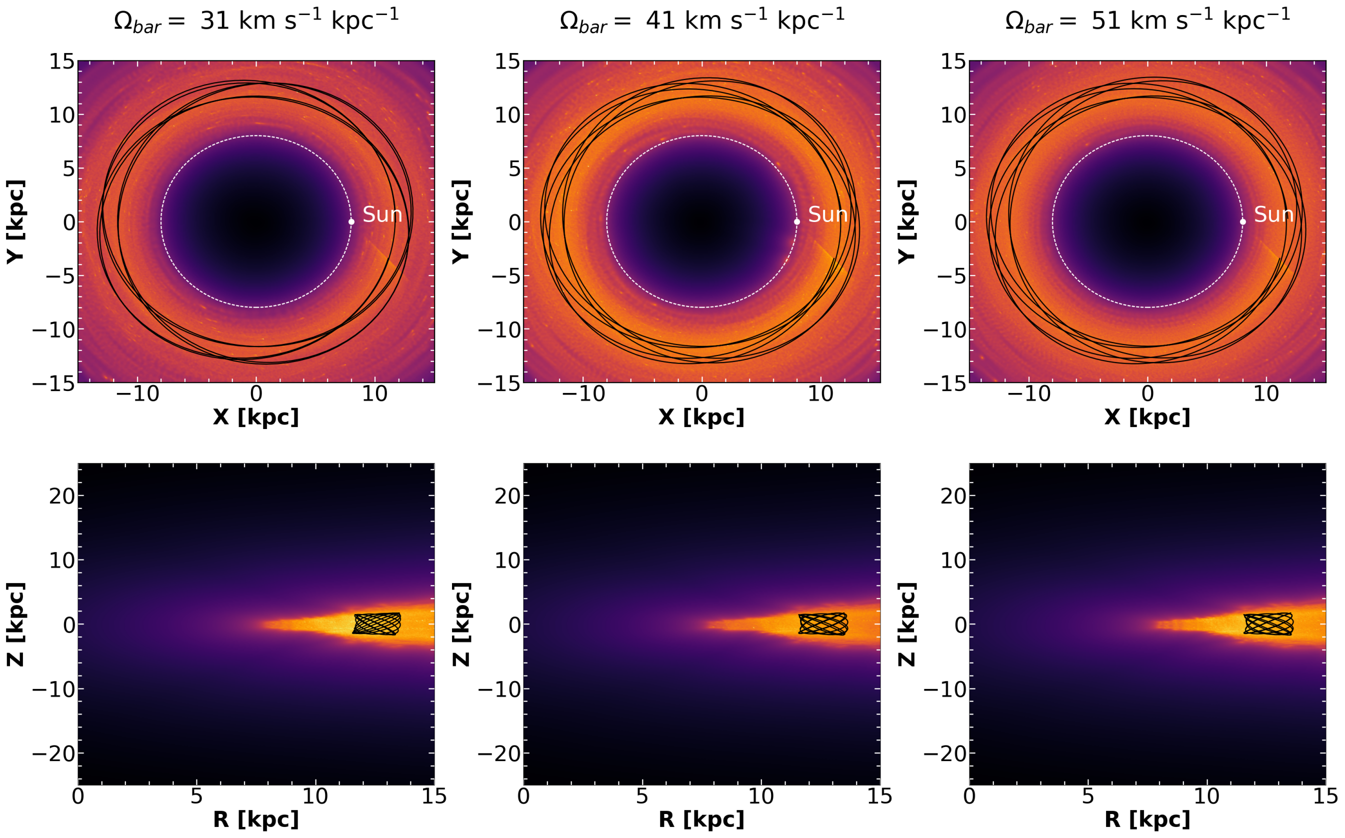

(c)

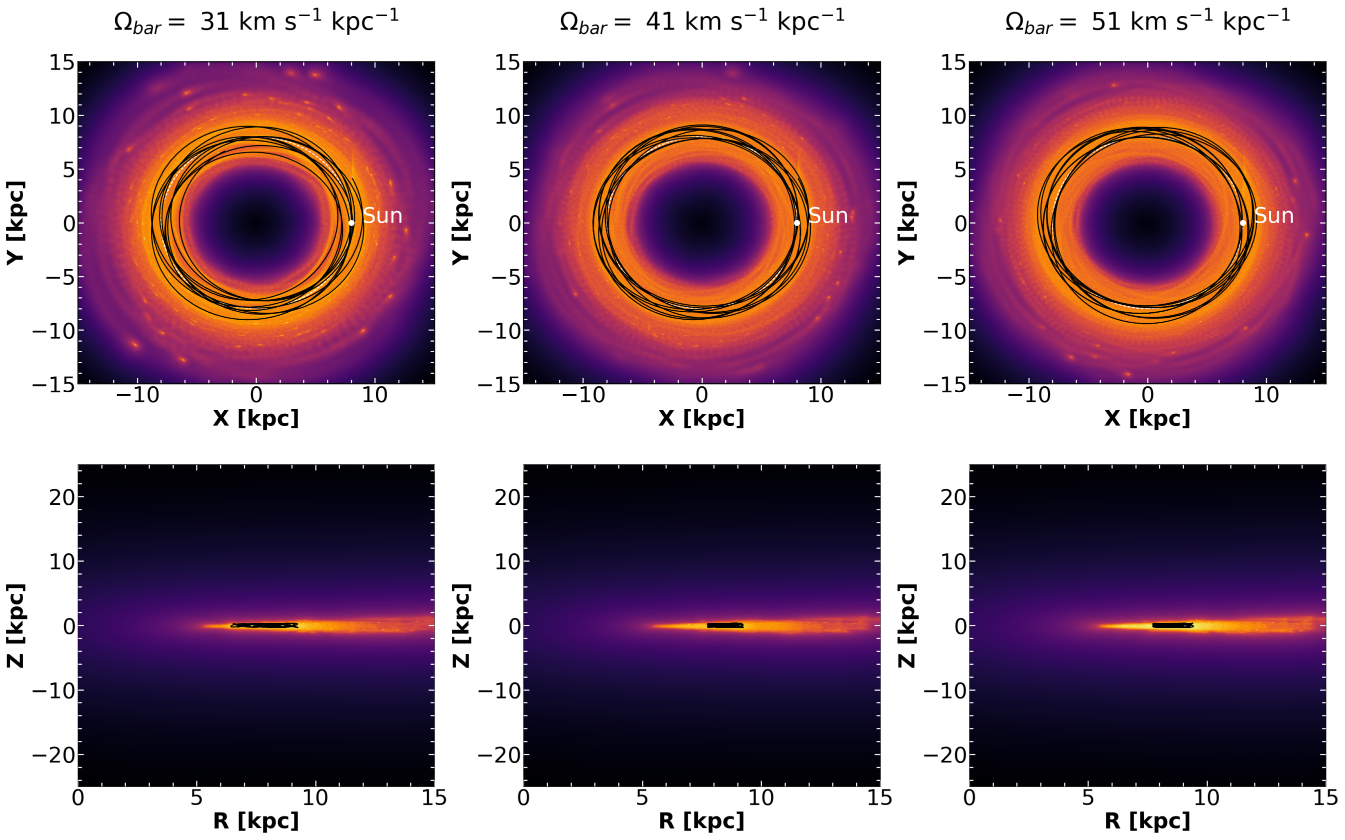

(d)

Fig. B.1. continued.

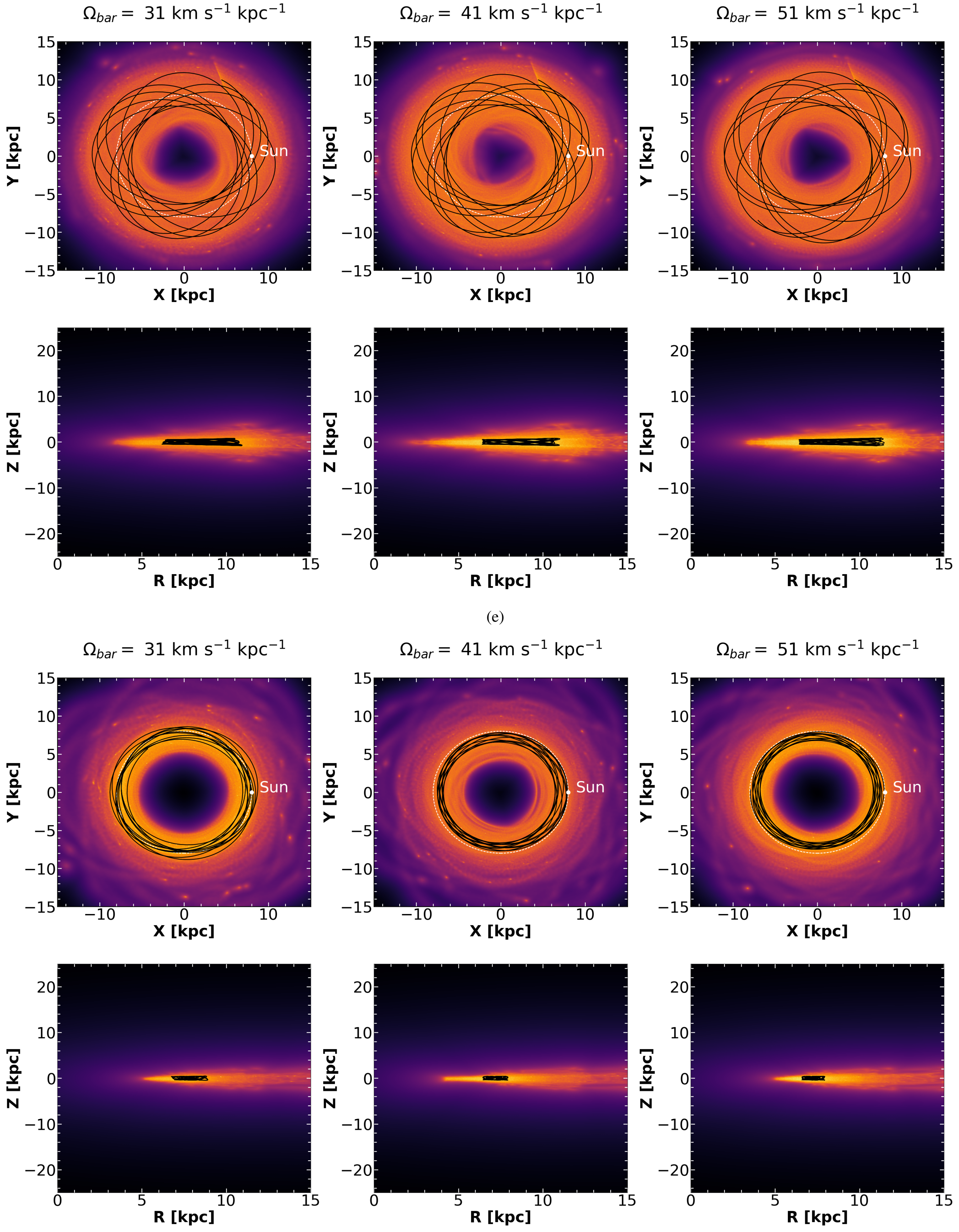

(e)

(f)

Fig. B.1. continued.

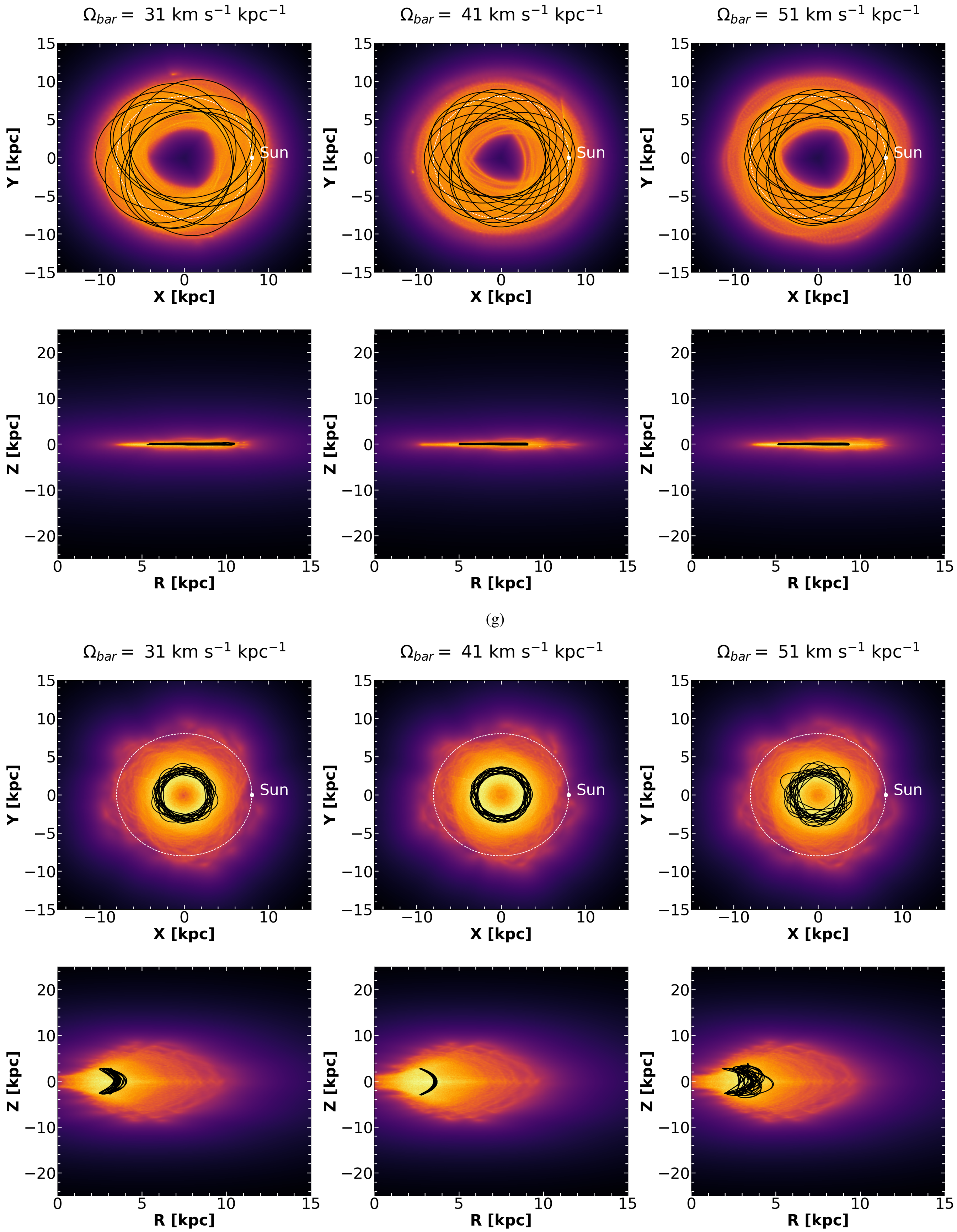

(g)

(h)

Fig. B.1. continued.

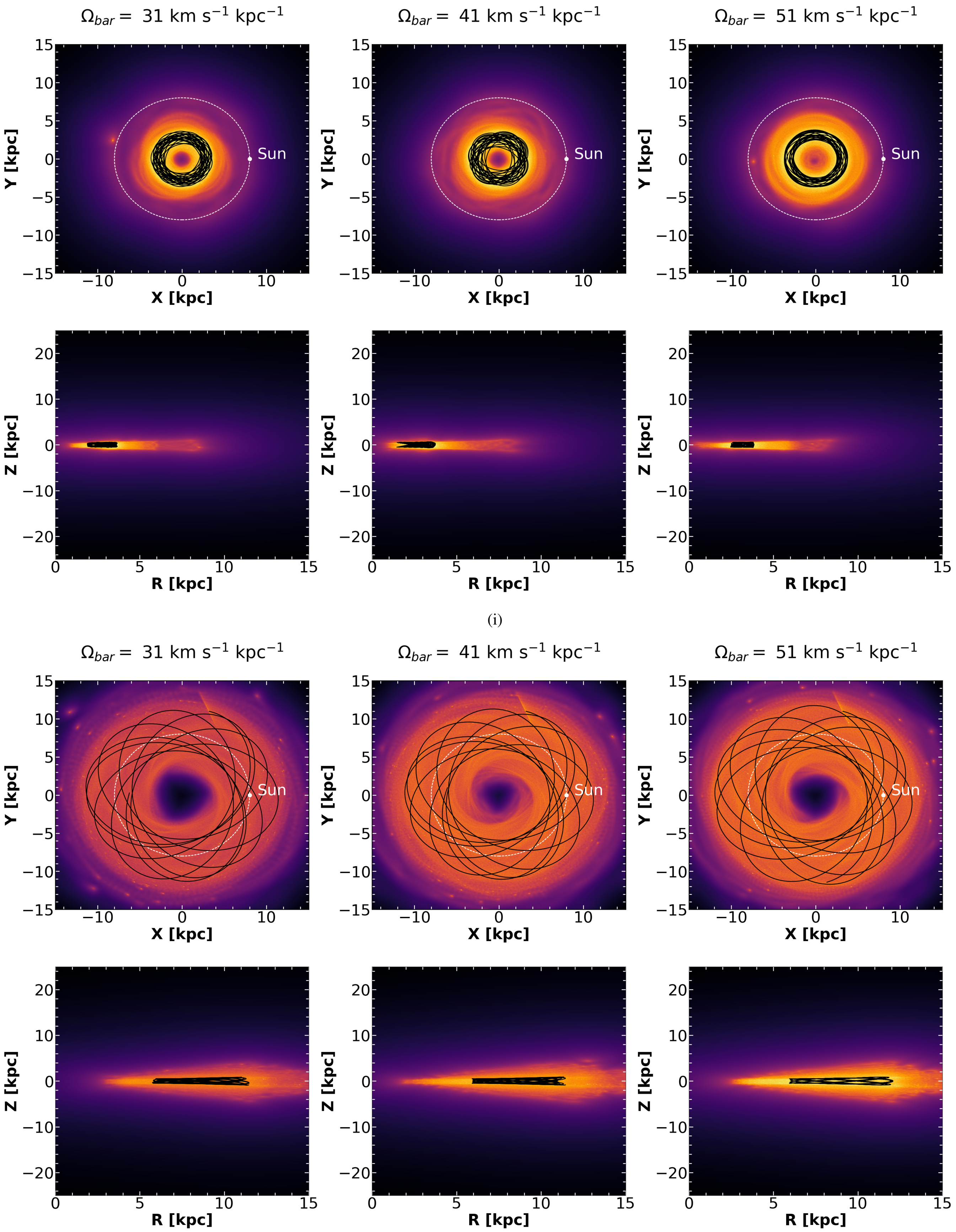

(i)

(j)

Fig. B.1. continued.

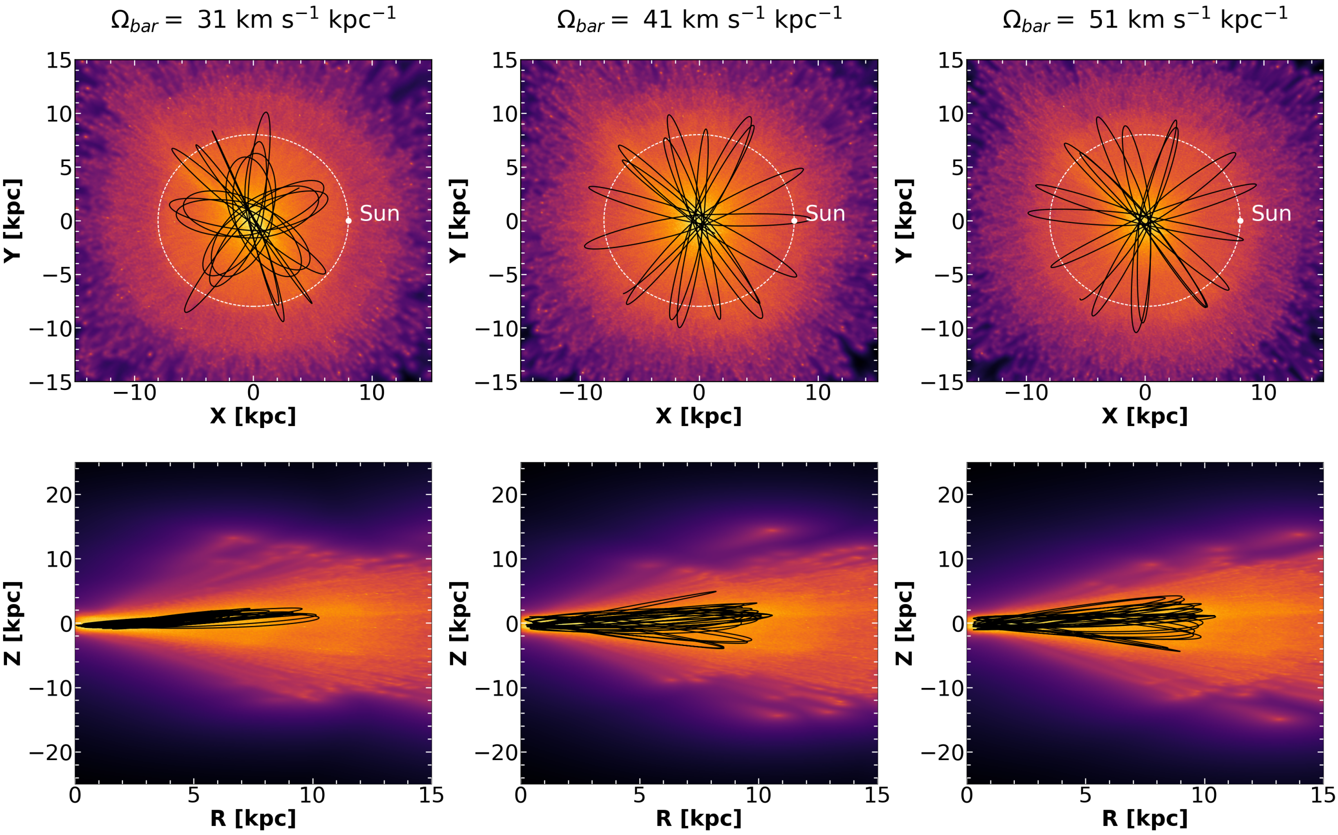

(k)

Fig. B.1. continued.